JGR Space Physics

RESEARCH ARTICLE

10.1029/2022JA030962

Key Points:

- Dissipation broadens amplitude(phase) latitudinal(vertical) structures with increasing height(latitude)
- Vertical wavelength shortening occurs with the shift to positive background thermal gradient above the mesopause
- Molecular dissipation and ion drag result in decreased amplitudes with increasing solar activity at 400 km

Supporting Information:

Supporting Information may be found in the online version of this article.

Correspondence to:

J. M. Forbes,
forbes@colorado.edu

Citation:

Forbes, J. M., & Zhang, X. (2022). Hough Mode Extensions (HMEs) and solar tide behavior in the dissipative thermosphere. *Journal of Geophysical Research: Space Physics*, *127*, e2022JA030962. https://doi.org/10.1029/2022JA030962

Received 29 AUG 2022
Accepted 31 OCT 2022

Hough Mode Extensions (HMEs) and Solar Tide Behavior in the Dissipative Thermosphere

Jeffrey M. Forbes[1] and **Xiaoli Zhang**[1]

[1]Ann and H.J. Smead Department of Aerospace Engineering Sciences, University of Colorado Boulder, Boulder, CO, USA

Abstract This paper quantifies and interprets how thermosphere dissipation in the form of molecular viscosity, molecular thermal conductivity and collisions with ions ("ion drag") determines the height versus latitude structures of a variety of migrating and non-migrating solar thermal tides, pole-to-pole up to 400 km altitude. This is done through computation of thermosphere Hough Mode Extensions (HMEs); that is, solutions to the linearized momentum, thermal energy, continuity, state and hydrostatic balance equations wherein the horizontal structure of troposphere forcing for each HME corresponds to the eigenfunction (Hough function) of Laplace's tidal equation for a particular tidal mode, and the background state and thermosphere dissipation are specified for nominal solar minimum, average and maximum activity conditions. The broad features revealed, different for each HME, include changes in vertical(horizontal) structure with latitude(height), degree of vertical penetration to the middle and upper thermosphere, changes in vertical wavelength (λ_z) with height due to the transition in background thermal gradient around the mesopause, and insights into role of ion drag in determining tidal amplitudes and their solar cycle variability. The HMEs are particularly useful for fitting measurements of tides, and for estimating tidal fields beyond those dependent variables actually fit and including those outside the fitting domain. The HMEs reported here were created as part of the Ionospheric CONnection (ICON) mission to serve as observation-based lower boundary conditions for Thermosphere Ionosphere Mesosphere General Circulation Model-ICON. Access to the full set of HMEs in tabular and graphical form is provided.

1. Introduction

Solar thermal tides (hereafter "solar tides") arise from the cyclic heating of the atmosphere due to Earth's rotation. The major sources of heating are the absorption of infrared(ultraviolet) solar radiation by $H_2O(O_3)$ in the troposphere(stratosphere), the latent heating of condensation associated with the daily variation in tropical convection, and the absorption of extreme ultraviolet (EUV) radiation in the thermosphere. It is now widely accepted that much of the tidal spectrum excited in the troposphere and stratosphere propagates vertically, grows in amplitude exponentially with height, achieves maximum amplitudes mainly between 100 and 150 km, and exerts significant dynamic and electrodynamic influences on ionosphere-thermosphere ("IT") dynamics, chemistry and electrodynamics above 100 km (Forbes, 2021).

A major impediment to the advancement of our understanding and quantitative specification of atmosphere-IT coupling is the lack of adequate wind and temperature observations in the critical 100–250 km height region where the tidal spectrum evolves with height due to molecular dissipation and collisional interaction with the ionosphere. Forbes et al. (2022) present some first observational insights into semidiurnal tidal propagation between 100 and 250 km based on daytime wind measurements from the Michelson Interferometer for Global High-resolution Thermospheric Imaging (MIGHTI) instrument on the Ionospheric CONnections (ICONs) mission. However, these are confined to 61d-mean depictions over a restricted latitude range (9°S–39°N) due to the sampling constraints imposed by the ICON orbit.

To aid in understanding atmosphere-IT coupling in the context of tidal winds and temperatures measured by MIGHTI, and F-region plasma drifts and densities measured by the Ion Velocity Meter instrument on ICON, a hybrid data-theory approach (see e.g., Cullens et al., 2020; Forbes et al., 2017) has been implemented as part of the ICON mission. The methodology consists of several steps. First, tides are obtained within 45-day running windows, stepped forward one day at a time, by least-squares (LSQ) fitting day and night wind and temperatures measurements from MIGHTI over the ~95 to 105 km height and 12°S–42°N latitude region. The individual tides are then LSQ fit with two-dimensional (height vs. latitude, hereafter "htvslat") basis functions rooted in tidal theory, leading to a pole-to-pole observation-based specification of the tidal spectrum in the lower-thermosphere. The tidal spectrum is then transformed into the time domain and mapped onto the latitude × longitude × UT grid of the Thermosphere Ionosphere Mesosphere General Circulation Model-ICON (TIEGCM-ICON; Maute, 2017) at its 97-km lower boundary. Along with other inputs such as solar flux and parameterized high-latitude forcing, TIEGCM-ICON then provides global specifications of IT dynamics, electrodynamics and chemistry above 97 km altitude for interpretation of the ICON measurements. The daily TIEGCM-ICON outputs are provided as a Level-4 data product of the of the ICON Mission (ftp://icon-science.ssl.berkeley.edu/pub/LEVEL.4).

The basis functions for fitting tides are referred to as "Hough Mode Extensions (HMEs)" (Forbes & Hagan, 1982; Lindzen et al., 1977). Hough modes (HMs) are the eigenfunctions of Laplace's tidal equation (see e.g., Chapman & Lindzen, 1970, and references therein dating back to the nineteenth century), each defining latitude structures pertinent to the perturbation vertical velocity, temperature, density or pressure of that mode. Latitudinal structures of the corresponding eastward and southward perturbation winds are also derived from the HMs. Each HM has an associated eigenvalue ("equivalent depth") which provides a measure of its vertical wavelength (λ_z). Laplace's tidal equation arises from the linearized momentum, thermal energy, continuity, state and hydrostatic equations by assuming solutions that are periodic in time and longitude, consistent with the cyclic absorption of solar radiation due to planetary rotation noted previously. It assumes the tidal oscillations to be perturbations on a background atmospheric state (temperature (T_0), density (ρ_0), and pressure (p_0)) that is horizontally stratified (hence windless) and neglects dissipative process such as molecular diffusion that introduce second-order vertical derivatives in the horizontal momentum and thermal energy equations.

In the thermosphere, molecular dissipation exerts a dominating influence on the behavior of tides, and precludes a separable eigenfunction-eigenvalue approach to the problem. HMEs are numerical solutions to the linearized equations with molecular dissipation included (see e.g., Forbes & Garrett, 1979), but the assumption of horizontal stratification (which implies zero mean winds) is retained. HMEs are computed from Earth's surface to 400 km, and are forced with conveniently calibrated (but otherwise arbitrary) tropospheric heat sources with horizontal structures defined by the individual HMs of Laplace's tidal equation. From the surface to about 100 km, the HME solutions are identical to those obtained from the "classical tidal theory" noted above. However, above 100 km, each tidal component achieves a maximum at some altitude that is dependent on its period and λ_z (see Forbes & Garrett, 1979, for a review of earlier work on this topic). Moreover, its latitude structure varies with height, or equivalently, its height structure varies with latitude, in keeping with the "inseparability" of the tidal equations in the presence of molecular dissipation. The computation of HMEs is described in some detail in Section 2.

A key feature of each individual HME is that it maintains self-consistent amplitude and phase (hereafter "amp/phz") relationships between perturbation temperatures, winds, densities and geopotential heights. HME fitting involves finding a single complex normalizing factor that determines absolute amp/phzs for all variables that best fit the input data in a LSQ sense. In addition to the fitting to ICON data described above, HMEs have been fit to wind and temperature measurements from the Upper Atmosphere Research Satellite (Svoboda et al., 2005), the Thermosphere Ionosphere Mesosphere Energetics and Dynamics (TIMED) mission (Oberheide et al., 2011), and ground-based measurements (Forbes & Vial, 1991). The Svoboda et al. (2005) study used proxy data from a general circulation model to demonstrate and validate the veracity of the technique. In each case, the produced results have been month-to-month climatologies of tidal winds, temperatures and densities involving parameters beyond those that were fit, and extending to latitudes and heights outside the fitting domain. HMEs can moreover be used to aid in the interpretation of tidal measurements. The utility of HMEs to interpret tidal variations in densities and winds measured by the CHAMP satellite near 390 km is demonstrated by Oberheide et al. (2009), Häusler et al. (2012), and Forbes et al. (2021, 2022) demonstrate how HMEs can facilitate the interpretation of tidal winds in the 100–300 km height regime based on ICON/MIGHTI measurements.

While the above studies have illustrated the htvslat amp/phz structures of a limited number of HMEs, including a few examples of their solar cycle dependencies (Oberheide et al., 2011), the full scope of their behaviors has never been depicted and interpreted, and tabulations of HMEs have never been made publicly accessible. Several objectives of the present work are to update and expand the scope of HMEs that are computed, to document their computational details more specifically, to archive and make them publicly available for scientific use, and to provide sufficient physical insights so that users can make optimum use of the HMEs. At the same time, achievement of these objective presents the opportunity to provide new insights into tidal behavior in the thermosphere, including the range of htvslat structures that likely exist in the actual thermosphere, the effects of background thermal structure on tidal structures, solar cycle dependencies of tides that propagate into the thermosphere from below, and the role of ion drag. In the following section, the mathematical formulation and nomenclature of solar tides are reviewed and set into the present context, and details of how HMEs are computed are provided. In Section 3, the behaviors of solar tides in the dissipative thermosphere along with complementary physical insights are elucidated, many for the first time.

2. Mathematical Formulation of Solar Tides, Nomenclature and Computation of HMEs

The solar tidal heating distribution throughout the atmosphere can be expressed mathematically as

$$\sum_s \sum_n A_{n,s}(z,\theta)\left[\cos(n\Omega t + s\lambda - \phi_{n,s}(z,\theta)\right] \tag{1}$$

where t = universal time (UT), $\Omega = 2\pi \mathrm{d}^{-1}$, z = altitude, θ = latitude, integer n defines the tidal frequency, $A_{n,s}$ is the amplitude, and $\phi_{n,s}$ is the phase (i.e., longitude λ of maximum at 0000 UT, or UT of maximum at $\lambda = 0$), and integer s is the zonal wavenumber. The presence of the $s\lambda$ term recognizes that planetary rotation also admits periodicity with respect to longitude as well as to UT, and thus captures longitude variations that primarily arise from the influences of topography and land-sea differences on troposphere and stratosphere tidal heating. In this notation $s < 0 (s > 0)$ implies eastward(westward) propagation at a zonal phase speed $C_{ph} = -\frac{n\Omega}{s}$. "Zonally symmetric" ($s = 0$) tidal sources oscillate in unison at a given tidal frequency at all longitudes, and do not propagate zonally. A tide at any frequency with $s = n$ migrates westward with the apparent phase speed of the Sun ($-\Omega$) to a ground-based observer; these are solar-synchronous and often referred to as "migrating" tides. Solar asynchronous tides with $s \neq n$ are often referred to as "non-migrating" tides, and it is these tides that capture the longitude dependence of tidal sources. The notation DWs or DEs is used to denote a westward or eastward-propagating diurnal tide, respectively, with zonal wavenumber = s. For semidiurnal(terdiurnal) oscillations, "S(T)" replaces "D." The zonally symmetric oscillations are denoted D0, S0, and T0.

In a linear system, the individual responses to each of the source terms in the expansion (Equation 1) are independent of each other. Therefore if one assumes complex solutions of the form $f' \sim \hat{f} \exp i(n\Omega t + s\lambda)$ for the linearized momentum, thermal energy, hydrostatic, continuity and state equations, then the tidal responses (in terms of wind, temperature, density and pressure perturbations on an assumed horizontally stratified basic state) as a function of z and θ can in principle be obtained. The linearized tidal equations for calculation of the HMEs and their method of numerical solution are given in Forbes (1982). In that work, the linearized equations are consolidated into 4 second-order partial differential equations in the three wind components u', v', w' (eastward, southward and vertical) and temperature T' with respect to colatitude (3°, pole to pole) and height (0 to approximately 400 km). A stretched variable (x) is defined to enable different vertical resolutions in the boundary layer, middle atmosphere and thermosphere that however remain the same for different levels of solar activity in the thermosphere; tabulations in the Supporting Information S2 are based on sampling the output in increments of ≈4 km. Subsequent to Forbes (1982) and Forbes and Hagan (1982), the HME calculations also included perturbation relative densities (ρ'/ρ_0) and geopotential heights $\left(\phi'_h\right)$. The perturbation densities are calculated from the continuity equation:

$$\frac{\partial}{\partial t}\left(\frac{\rho'}{\rho_0}\right) = -w'\frac{1}{\rho_0}\frac{d\rho_0}{dz} - \chi' \tag{2}$$

where χ' is the divergence of the perturbation velocity field. The geopotential heights are calculated from the linearized equation of state:

$$\frac{p'}{p_0} = \frac{\rho'}{\rho_0} + \frac{T'}{T_0} \tag{3}$$

as follows:

$$\phi'_h = \frac{p'}{\rho_0 g} = H\frac{\rho'}{\rho_0} + H\frac{T'}{T_0} \tag{4}$$

where g is the acceleration due to gravity. In complex form, we have:

$$\frac{\hat{\rho}}{\rho_0} = \left(-\hat{w}\frac{1}{\rho_0}\frac{d\rho_0}{dz} - \hat{\chi}\right)/in\Omega \tag{5}$$

$$\hat{\phi}_h = \frac{\hat{p}}{\rho_0 g} = H\frac{\hat{\rho}}{\rho_0} + H\frac{\hat{T}}{T_0} \tag{6}$$

See Forbes (1982) for additional details regarding boundary conditions, method of numerical solution, and so forth.

The model used to create the HMEs is identical to that described in detail in Forbes (1982), except for the assumed background ionosphere and neutral atmosphere, and the thermal forcing. In the present implementation, each HME is forced with a heat source confined to the troposphere, and with latitude shape given by the corresponding HM.

The HMs corresponding to the HMEs in the current work were first depicted graphically in Truskowski et al. (2014), along with estimates of their vertical wavelengths based on the eigenvalues corresponding to each HM and an assumed isothermal background atmosphere of $T_0 = 256$ K. The HMs and eigenvalues were calculated using the same basic methodology as outlined in Chapman and Lindzen (1970), and many were validated against a range of independently determined values (e.g., Flattery, 1967; Longuet-Higgins, 1968). The Supporting Information S2 to this paper contains tabulations of these HMs and eigenvalues, and eastward and southward wind expansion functions that are derived from the HMs. The heat source for each HME of given n, s is arbitrarily normalized to yield an equatorial temperature amplitude of 10 K at 98 km for a 10.7-cm solar flux (F10.7) of 75 sfu. The same heat source is used for all HMEs of a given n, s, which means there can be very small differences from the 10 K value at 98 km for other levels of solar activity. The phase at 98 km is also arbitrary, determined by the vertical wavelength of the oscillation and by the arbitrarily chosen phase of heating (UT of maximum at 0° longitude). Amps/phzs of all other variables at all other heights and latitudes are consistent in a relative sense to this normalization, in keeping with the HME solutions described in the previous subsection.

The same mathematical formulations of molecular and thermal conductivities, and ion drag coefficient, used in Forbes (1982) are adopted in the current work. However, the neutral atmosphere and ionosphere models used in Forbes (1982) are replaced by the NRLMSIS2.0 model (Emmert et al., 2020) and the analytic Chiu (1975) model, respectively. In keeping with the horizontally stratified nature of the background neutral atmosphere, the local time, longitude, and intra-annual variations within NRMLMSIS2.0 are suppressed, reducing the neutral density and temperature specifications for the HMEs to an annual- and diurnal-mean specification at the equator; this also implies a windless basic state. The 10.7-cm solar flux unit (sfu) values input into the model, namely F10.7 = 75, 100, 125, 150, 175, and 200 sfu, translate to exosphere temperatures of 753, 853, 943, 1024, 1096, and 1159 K. The corresponding temperature profiles are illustrated in Figure 1. In this paper we will also refer to F10.7 = 75 and F10.7 = 175 sfu as representing nominal solar minimum (SSMIN) and solar maximum (SSMAX) conditions.

Similarly, the ion drag coefficient in the momentum equations consists of a single average profile for each level of solar activity, based on diurnal-mean electron density profiles at 0° longitude, and averaged between −30° and +30° latitude. This choice is consistent with the low-latitude extent of many of the low-order HMEs that extend to high altitudes. The corresponding ion drag coefficients ϵ_0 are also provided in Figure 1. Given the simple way that the background atmosphere and ionosphere are implemented in the model, use of the HMEs in scientific studies must keep these simplifications in mind.

The ϵ_0 maxima and their corresponding altitudes in Figure 1 increase with F10.7 in concert with the F-region maxima in electron density (N_m) and their corresponding altitudes (h_m) (not shown). Notably, between about 160 and 260 km, ϵ_0 at SSMIN exceeds that at SSMAX, whereas the reverse is true above ∼280 km. The impacts of this height dependence of the solar cycle variability of ion drag is discussed in subsection 3.3. The factors behind the changes in N_m and h_m (and hence ϵ_0 vertical profile) variations with solar activity are the rates of photo-production (q), chemical loss (L), and plasma diffusion (D) which act together symbiotically in response to increasing solar flux, neutral densities and plasma scale height (H_p) with solar activity (see e.g., Rishbeth & Garriott, 1969). The approximate location of daytime h_m is where the time constant for diffusion (τ_D) equals the time constant for chemical loss (τ_L), where $\tau_D = H_p^2/D \propto H_p^2[O]$ and $\tau_L \propto 1/[N_2]$ for an O-N$_2$ thermosphere;

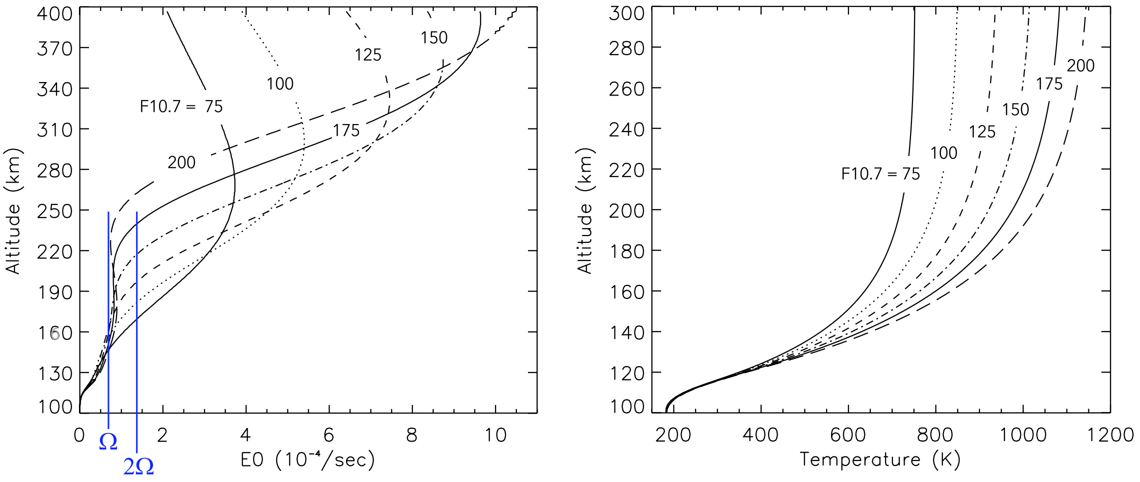

Figure 1. Vertical profiles of ion drag coefficient (E0, or ϵ_0 in the text, left) and background temperature (right) adopted in the study for different levels of 10.7 cm solar radio flux (F10.7, in sfu). The ion drag coefficients are based on electron densities from the Chiu (1975) analytic model and neutral densities from NRLMSIS2.0. The temperature profiles are based on NRLMSIS2.0. Details on how each profile was obtained is provided in the text. Diurnal and semidiurnal tidal frequencies are indicated in the left figure, where $\Omega = 2\pi d^{-1}$.

$N_m \approx q_m/L_m$ where subscript m denotes values at h_m. (The values of N_m and h_m are modified at night and/or in the presence of vertical drifts.) Since τ_D = decreases exponentially with height but increases with increasing solar activity, whereas τ_L increases exponentially with height but decreases with increasing solar activity, h_m increases with increasing solar activity. N_m increases with solar activity due to both the increase in q_m and decrease in L_m.

In the absence of a GW parameterization scheme, the effects of eddy diffusion are generally included in dynamical models of the middle and upper atmosphere to account for turbulence-induced transport of constituents, momentum and heat. However, controversy and uncertainty still surround the choice of eddy diffusivity (hereafter K_{eddy}). In the HME calculations, a single K_{eddy} profile with peak near 200 m^2s^{-1} is assumed, a magnitude consistent with the arguments put forth in Forbes (1982), Lindzen and Forbes (1983), and more recent estimates based on similarity theory and measurements of energy dissipation rates (Vlasov & Kelley, 2015). A turbulent Prandtl number of unity is assumed, meaning that the values of momentum eddy diffusivity and heat transfer eddy diffusivity are equal. Given the uncertainties involved, and to understand the implications of the above voice of K_{eddy}, experiments with similar-shaped profiles with maximum K_{eddy} values ranging between 50 and 500 m^2s^{-1}, viewed as lower and upper extrema, were performed with respect to DW1. (These profiles appear in Figure S1 in Supporting Information S1.) DW1 is particularly susceptible to eddy dissipation due to its relatively short vertical wavelength (~30 km) and long period compared to other tides. Over this range of values, with the exception of the $K_{\text{eddy}} = 500\ \text{m}^2\text{s}^{-1}$ case, the DW1 amp/phz profile shapes with respect to height and latitude did not differ much above 100 km, but the peak values of eastward wind (e.g.) near 100 km ranged between 65 and 105 ms^{-1}. This difference is the result of dissipation effects integrated over about 70–100 km between the various K_{eddy} profiles. Due to this dependence on choice of K_{eddy}, HMEs with λ_z ~30 km should be used with this caveat in mind. A few examples and discussion pertinent to this point are provided in Section 3.

Due to their higher frequencies, semidiurnal and terdiurnal tides are somewhat less sensitive to the choice of K_{eddy}. More importantly, it is characteristic of tides with λ_z ~30 km or less to peak near 100 km altitude and to decrease rapidly above this height. The focus of the present paper is on tides that originate from lower altitudes and that effectively penetrate into the thermosphere. Therefore, with a few exceptions that are included for completeness, the present study only considers thermosphere extensions of tidal modes with $\lambda_z \gtrsim 30$ km. This also implies that most of the HMEs calculated and presented as part of this study are robust with respect to the choice of eddy diffusivity described above. A few exceptions will be noted later.

Hereafter in this paper, we will use capitalized U, V, T to denote eastward and southward winds and temperatures, respectively, associated with HMEs. The HMEs that accompany the current work include DE3, DE2, DE1, D0, DW1, DW2, SE3, SE2, SE1, S0, SW1, SW2, SW3, SW4, SW6, and TW3. These tides all appear in multi-year mean tidal determinations from lower-thermosphere observations from the TIMED mission (e.g., Oberheide et al., 2011; Truskowski et al., 2014). The reader is referred to Truskowski et al. (2014) concerning current thinking on the origins of these tides. In addition to HMs and related quantities based on solutions to Laplace's tidal equations, the Supporting Information S2 accompanying this paper includes htvslat plots of U, V, and T amp/phzs of the aforementioned HMEs, and model outputs that include tabulations of amp/phzs of perturbation densities ($\Delta\rho/\rho_0$) and perturbation geopotential heights ($\Delta\Phi_h$) in addition to U, V, and T. For each tide, results are provided that correspond to F10.7 = 75, 125, and 175 sfu, and for the largest tides reaching the upper thermosphere (SW2, DE3, and SE2), results corresponding to F10.7 = 100, 150, and 200 sfu are additionally provided. In addition, output files for "legacy" HMEs which were utilized to construct the Climatological Tidal Model of the Thermosphere (CTMT) as described in Oberheide et al. (2011), and all other papers that have utilized HMEs to date, are included in a separate directory. These legacy HMEs correspond to F10.7 = 110 sfu, and employ earlier versions of background thermosphere and ionosphere parameters as described in Forbes (1982). However, they may prove useful to those seeking consistency with tidal structures contained in the CTMT, or other earlier papers that employed HMEs.

The following section provides a review of the physical characteristics of HMEs and their interpretation based on a limited sample of HMEs. It is intended to provide potential users with sufficient knowledge such that HMEs can be potentially useful in their research. It so happens that it also reveals aspects of mesosphere-thermosphere tidal propagation that have never been discussed in the literature before.

3. Results

3.1. Diurnal Tide HMEs

The htvslat structures of amp/phz of U, and amplitude of V, for HME-1 of DE3, DE2, and DE1 corresponding to F10.7 = 125 sfu are depicted together in Figure 2. Each of the tides depicted in Figure 2 were normalized to possess maximum temperature amplitudes of 10 K at the equator. This is an arbitrary choice based on convenience and consistency for the current presentations, and the displayed amplitudes should therefore not be construed as appropriate for direct comparison with observational data. These symmetric HMEs represent the thermospheric extensions of Kelvin wave solutions to Laplace's tidal equation. They belong to the class of "ultra-fast Kelvin waves" (UFKWs; Salby et al., 1984) with periods of $\lesssim$5 days that are known to propagate to lower thermosphere heights based on observations (Forbes, He, et al., 2020; Gu et al., 2014; Liu et al., 2015) and modeling (Forbes, Maute, & Zhang, 2020; Pancheva et al., 2016). As such, they have familiar features, such as latitudinal structures centered on the equator for U and T that are Gaussian-shaped with widths that decrease with increasing zonal wavenumber; southward winds (V) that are antisymmetric about the equator and comparatively small in magnitude compared with U; and λ_z that decrease with increasing wave period.

The λ_z for DE3, DE2, and DE1 based on their phase progressions with height between 70 and 98 km (designated nominal height of 84 km) are 57, 224, and 2,036 km (see column (a) of Table 1). Since molecular dissipation varies inversely with λ_z^2, DE3, DE2, and DE1 therefore show increasing capacity to penetrate further into the thermosphere, as indicated by the U amplitudes in Figure 2a, d and g. However, the aforementioned λ_z are not completely representative of their capacities to do so. As reflected in the distances between lines of constant phase, for each of these tides their λ_z undergo a transition in the vicinity of 100 km, decreasing to smaller values (reflected in more compressed phased contours) before increasing once again above 150 km. This is counter-intuitive to the notion that as a tide propagates into the thermosphere, that its phase progression decreases monotonically with increasing height and eventually approaches zero (no phase with height) in the upper thermosphere; that is, vertical diffusion of heat and momentum is so fast that vertical gradients in horizontal winds and temperature cannot exist in the absence of local sources. As explained below, the transition near 100 km reflects the influences of changes in the background thermal structure below and above the mesopause, and is a feature of thermosphere tidal propagation that has not been highlighted or interpreted before.

Another feature of these "diurnal Kelvin wave" phase structures in the thermosphere, above about 120 km, is that the λ_z increase with latitude. This is accompanied by an increased latitudinal broadening of the Gaussian shape of U with height. These features reflect the height-latitude inseparability of the tidal equations in the dissipative thermosphere. Note that the U amplitudes of DE1 extend to the poles, since continuity over the poles permits existence of $|s = 1|$ oscillations there (Hernandez et al., 1992, 1993). Nevertheless, this is a surprising manifestation of a "Kelvin wave," which is typically viewed as an oscillation that is confined to low latitudes. A similar

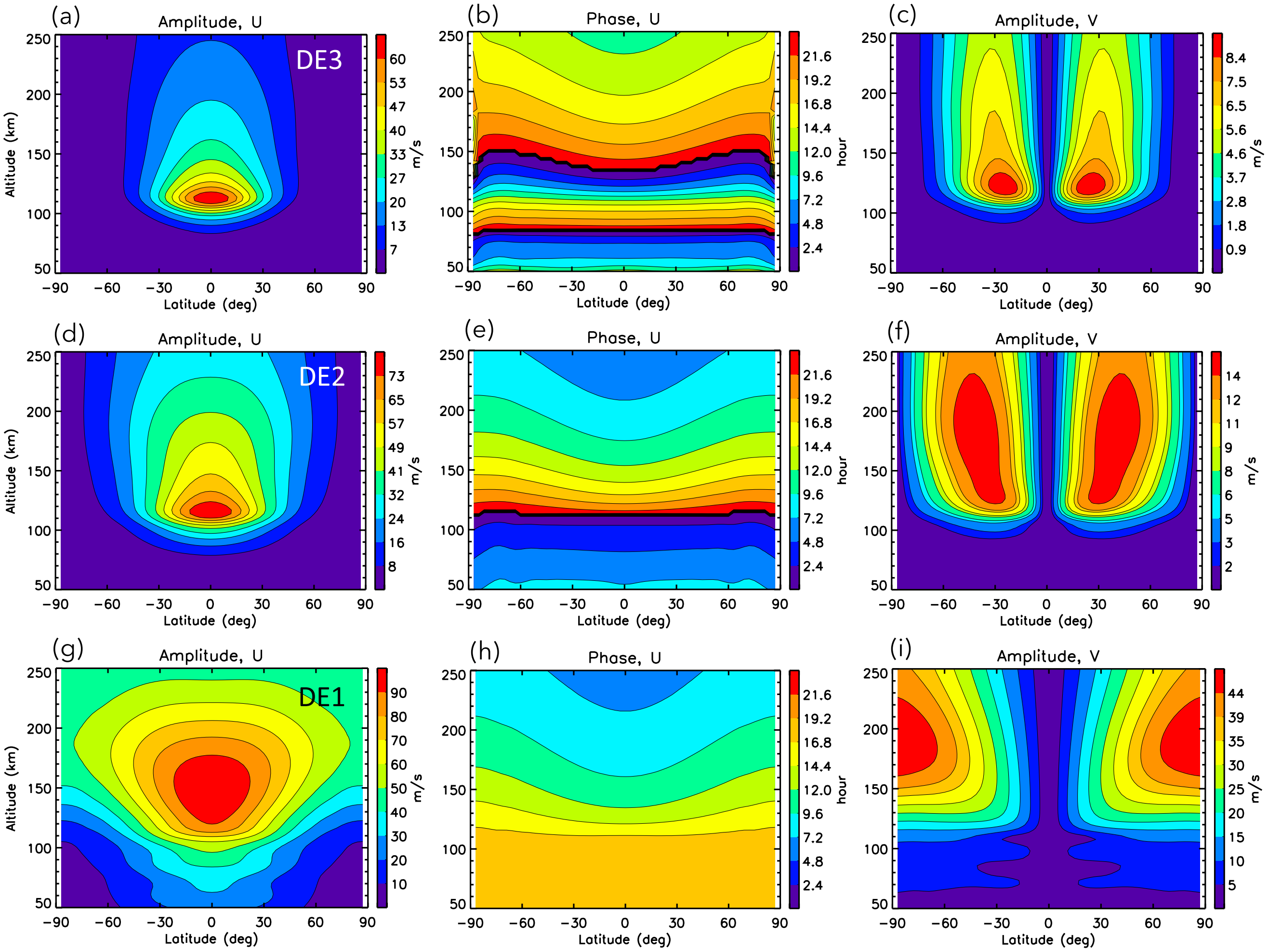

Figure 2. Height versus latitude distributions of amplitude of U (left), phase of U (middle), and amplitude of V (right) for HME1 of DE3 (top), DE2 (middle), and DE1 (bottom) corresponding to F10.7 = 125 sfu.

discovery was made by Forbes (2000) in connection with the 3D UFKW with $s = -1$. Another interesting aspect of DE1 is that the V amplitudes in the thermosphere are about one-half those of U, in contrast to DE2 and DE3, which have comparatively small amplitudes relative to U.

HME1 for the D0 tide corresponding to F10.7 = 125 sfu is considered in Figure 3, where htvslat amp/phz structures are presented for U, V, and T. The reader is reminded that for zonally symmetric oscillations, the fundamental mode is antisymmetric. The vertical wavelength of D0 HME1 at 84 km is 174 km (column (a) of Table 1). The effects of dissipation on the htvslat structures of D0 HME1 are similar to those noted above for the diurnal UFKW HMEs; that is, latitudinal broadening of with increasing height, phase compressions just above 100 km, and increased vertical stretching of phase contours with increasing latitude. Specific to D0, note that while non-zero U and V are permitted over the poles for $|s = 1|$ oscillations, non-zero T (as well as $\Delta\rho/\rho_0$ and $\Delta p/p_0$) satisfy continuity over the poles for $s = 0$. The major departure that occurs in the horizontal structure of T, which shifts from maxima near ±30° latitude at 120 km altitude and below, to maxima at the poles at about 160 km and above, is the D0 analog to DE1 wind maxima over the poles.

Table 1
DE3, DE2, DE1, and D0 λ_z Based on Hough Mode Extension (HME) U Phases Over 70–98 ("84 km") and 102–122 km ("112 km"), Compared With Those Calculated Based on Equivalent Depths From Laplace's Tidal Equation (LTE) for a T_0 = 256 K Isothermal Atmosphere, and With Those Based on Equation 7 in the Text for a Non-Isothermal Atmosphere

	HME1					HME2	
	(a)	(b)	(c)	(d)	(e)	(f)	(g)
Tide	HME 84 km	LTE 256 K	LTE 84 km	HME 112 km	LTE 112 km	HME 84 km	LTE 256 K
DE3	57	56	59	40	35	30	30
DE2	224	108	164	64	56	38	38
DE1	2,036	∞	∞	145	90	54	53
D0	174	102	145	64	55	29	27

Note. ∞ implies no phase progression with height.

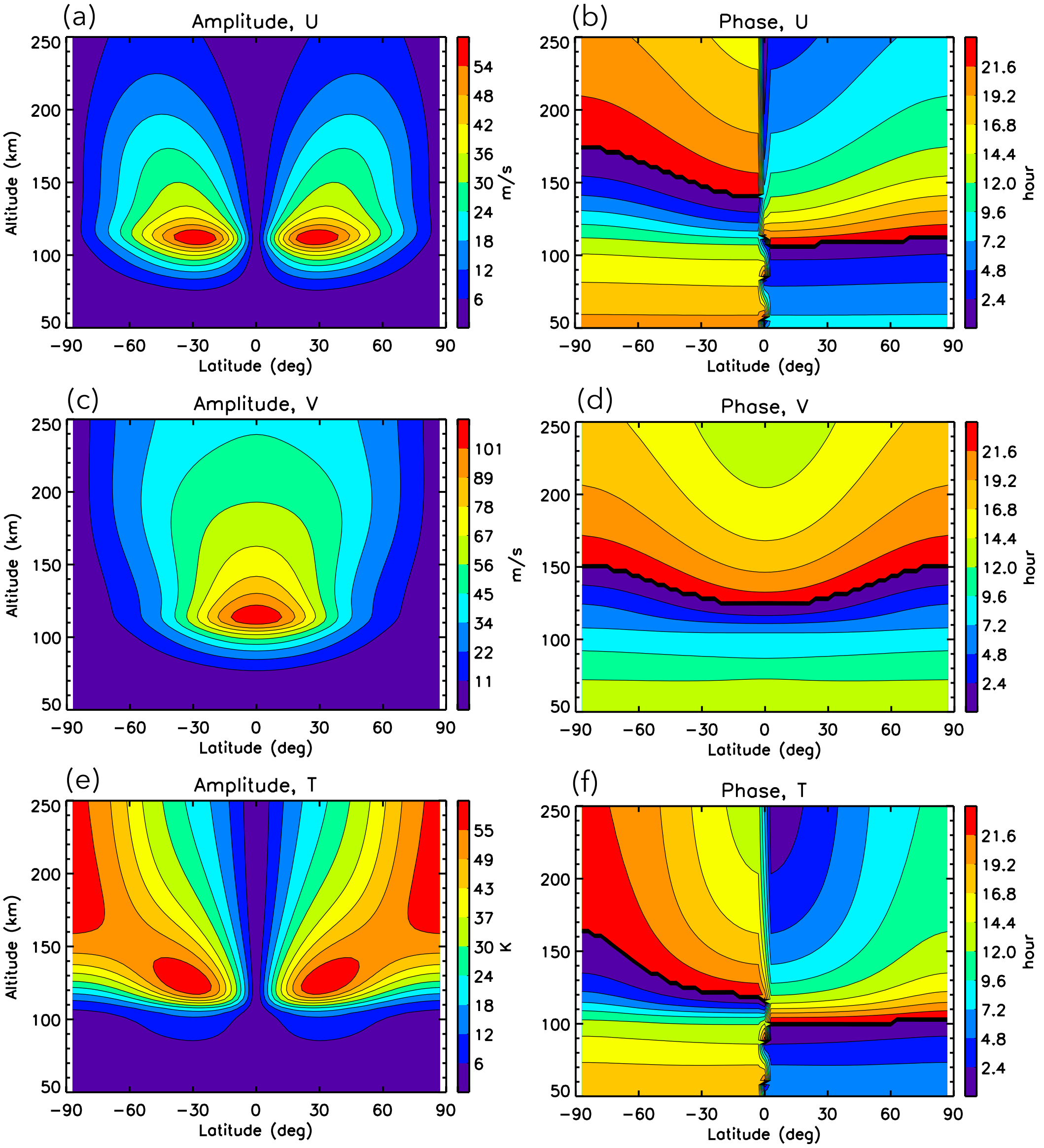

Figure 3. Height versus latitude distributions of amplitude (left) and phase (right) of U (top), V (middle), and T (bottom) for HME1 of D0 corresponding to F10.7 = 125 sfu.

It is also noted from Figures 2 and 3 that V amplitudes tend to peak at a higher altitude than U, and extend more extensively to higher altitudes above the peak than U. This is attributable to the influence of ion drag, which appears through the term $\epsilon_0 U$ in the eastward momentum equation, but is of diminished importance to V in the southward momentum equation (especially at low to middle latitudes) where the magnetic dip angle (I) enters through the term $\epsilon_0 V \sin^2 I$. Additional influences of ion drag are discussed in subsection 3.3.

HME2's for DE3, DE2, DE1, and D0 possess λ_z of 30, 38, 54, and 29 km at 84 km altitude (column (f) of Table 1). Due to the short λ_z for DE3, DE2, and D0 HME2s, these modes are not expected to play a significant role in vertically coupling the thermosphere. This means that the dominant manifestations of DE3 and DE2 should be symmetric about the equator, and the dominant manifestation of D0 is expected to be antisymmetric. For DE1, its vertical growth from a tropospheric source to 100 km is curtailed by the thermal structure of the atmosphere, which might imply that its dominant manifestation might be antisymmetric. This point is made and quantified immediately below, along with further insights into the vertical structures of HME1s and HME2s for these tides.

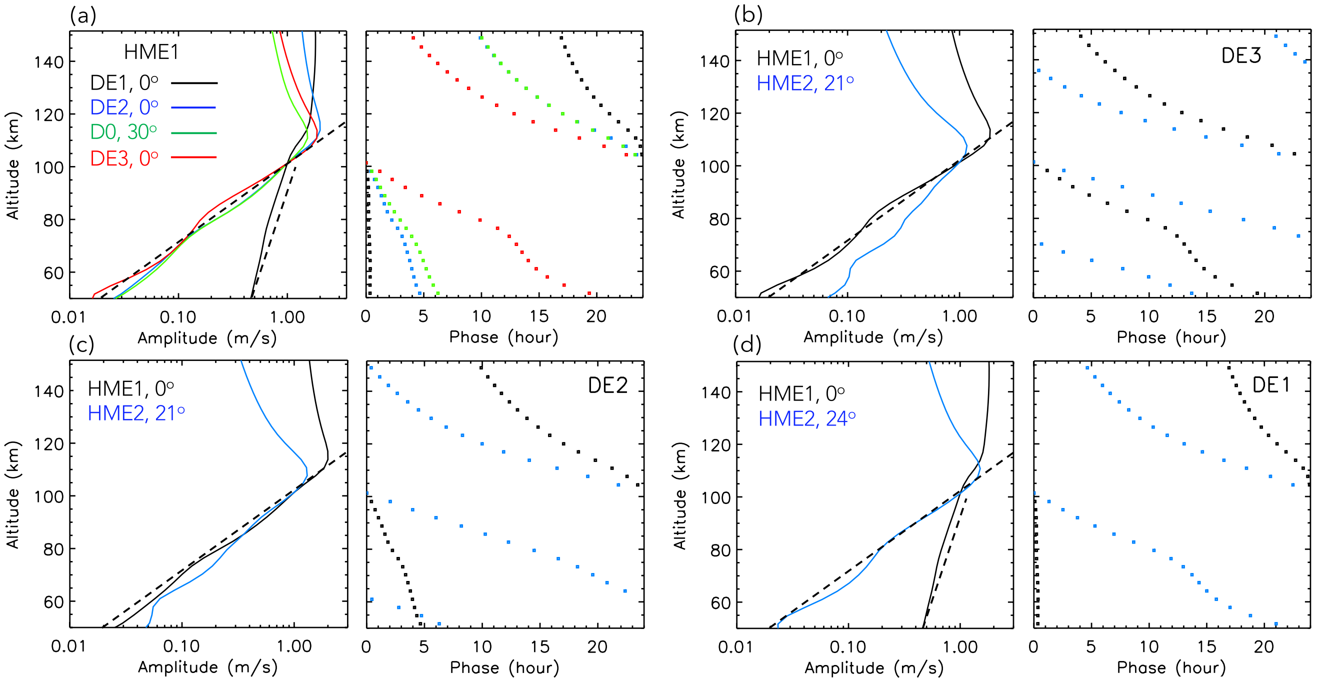

Figure 4. Amplitude and phase vertical profiles of U corresponding to F10.7 = 125 sfu for the Hough Mode Extensions (HMEs) and diurnal tides indicated in the panels: (a) HME1 for DE3, DE2, DE1, DO; (b) HME1 and HME2 for DE3; (c) HME1 and HME2 for DE2; and (d) HME1 and HME2 for DE1. Amplitudes are normalized to unity and phases are normalized to 0000 hr at 102 km, at the latitudes where maximum amplitudes occur, as indicated in each amplitude panel. Dashed lines indicate amplitude growth calculated from classical tidal theory.

To further understand the vertical amp/phz structures depicted in Figures 2 and 3, classical tidal theory (e.g., Chapman & Lindzen, 1970) is employed. In classical tidal theory, solution of the vertical structure equation generally takes a form proportional to $\exp(1/2 + i\alpha)x$ where x is the log-pressure coordinate, and

$$\alpha = \sqrt{\frac{H}{h_{n,s}}\left(\kappa + \frac{dH}{dz}\right) - \frac{1}{4}} \tag{7}$$

is a vertical wavenumber from which a vertical wavelength λ_z can be calculated: $\lambda_z = 2\pi H/\alpha$. In Equation 7 $\kappa = R/c_p = 2/7$, H is the scale height of the background atmosphere, $h_{n,s}$ is the equivalent depth (eigenvalue) of the associated HM, and where we have inserted the relation $dz = Hdx$ where z is altitude for later convenience. To simplify the presentation below and to capture the essence of the vertical structures that accompany various HMs, it suffices to calculate λ_z for an isothermal atmosphere (e.g., 256 K or $H = 7.5$ km) so that there is just one λ_z per HM. Note that this also implies that $x = z/H$.

In Figure 4, plots illustrating vertical profiles of U amp/phz of select diurnal HMEs corresponding to F10.7 = 125 sfu are presented. In Table 1, the λ_z calculated from classical tidal theory for an isothermal atmosphere (column (b)) are additionally provided for comparison with the U HME phase progressions between 70 and 98 km (column (a)). Agreement between the two values is quite good, except for DE2 HME1 and D0 HME1, for which the HME values are ~twice those computed for an isothermal atmosphere. This is due to neglect of the height dependence of H, which preferentially affects the waves with larger $h_{n,s}$. The influence of height-dependent H is discussed more specifically further below. For now, consider the influence of $h_{n,s}$ on the vertical amp/phz structure given by $\exp(1/2 + i\alpha)z/H$, which can take several forms enumerated below:

1. $h_{n,s} = \infty$: Sufficiently large $h_{n,s}$ yield $\alpha \approx i\frac{1}{2}$, which negates the $\exp(z/2H)$ exponential growth. The solution has constant amplitude with height and no phase change with height.
2. $h_{n,s} < 0$: Here $\alpha \rightarrow i|\alpha|$ where $|\alpha| > \frac{1}{2}$; $\exp(z/2H)$ is more than offset, resulting in a decaying solution with height with no phase change with height.
3. $h_{n,s} < 4\kappa H$: Sufficiently small positive $h_{n,s}$ yield positive values for α, implying vertical propagation, downward phase progression, and $\exp(z/2H)$ growth with height. This is the case for DE3, DE2, and D0 HME1s below

about 100 km, as illustrated in Figure 4a. All three tides share the same exponential amplitude growth with height, that is, $\exp(z/2H)$ where $H = 6.0$ km. Note that for longer λ_z the peaks maximize higher in altitude, and the tide penetrates more effectively to greater heights.

4. $h_{n,s} > 4\kappa H$: Here $\alpha \rightarrow i|\alpha|$ where $|\alpha| < \frac{1}{2}$. There is no phase progression with height below 100 km, and $\exp(z/2H)$ growth is only partially offset. This is the case for DE1 in Figure 4a. Here the dashed line calculated according to classical theory corresponds to $\exp(0.09z/H)$ based on the calculated value of $\alpha = 0.41i$, $i = \text{sqrt} - 1$, where $H = 6.0$ km and $dH/dz = -0.041$.

Figures 4b–4d compare HME1 and HME2 for DE3, DE2, and DE1, respectively. For DE3 (Figure 4b), a departure from $\exp(z/2H)$ growth exists for HME2. Recalling the cautionary remarks made previously, this reflects the effect of eddy diffusion on HME2 for DE3, which possesses a λ_z of 30 km (Table 1, column (f)). However, for DE2 HME2 with λ_z of 38 km (Figure 4c, Table 1, column (f)), the departure from unimpeded growth is minimal, reflecting the dependence of this type of dissipation on $1/\lambda_z^2$. The behavior of HME2 for D0 (not shown) with λ_z of 29 km (Table 1, column (f)), is similar to that of HME2 for DE3, except the departure is slightly greater. It can be concluded from the above that many diurnal tides enter the thermosphere at 100 km with the same $\approx \exp(z/2H)$ exponential growth, despite a wide range of λ_z. The exceptions are those with $h_{n,s} \lesssim 0.80$ km ($\lambda_z \lesssim 30$ km), whose growth is impeded by $K_{eddy} \gtrsim 200\ \mathrm{m^2 s^{-1}}$, and those with $h_{n,s} \gtrsim 6.0$ km ($\lambda_z \gg 100$ km) whose exponential growth is offset due to influences of the background temperature. This latter point has never been mentioned in the literature before, since the importance of non-migrating tides to dynamical coupling in the upper atmosphere has only been realized in the past few decades. It means that while lower-atmosphere sources might project efficiently onto such tidal modes in the lower atmosphere, their curtailed exponential growth may preclude them from being of practical importance in the thermosphere. It is a point to also be kept in mind when fitting HMEs to data in the lower thermosphere, especially when there is insufficient data coverage to distinguish some modes from others, for example, in the presence of latitude gaps. In unpublished work we have found that omitting the lowest-order HME from tidal fitting sometimes significantly improves the fit and the subsequent tidal reconstruction. In the following subsection, these topics are revisited in the context of semidiurnal and terdiurnal tides.

Concerning the reductions in λ_z with height above about 100 km that were noted in connection with Figures 2 and 3, we note that in Figure 4 this effect is obviously present for the longer-λ_z HME1 DE2, DE1, and D0, and nonexistent for the shorter-wavelength HME1 DE3 and all 4 HME2s. Calculating Equation 7 as before and with $\lambda_z = 2\pi H/\alpha$, LTE values of λ_z for DE2 and D0 of 164 and 145 km are now obtained (Table 1, column (c)), in much better agreement with the HME values of 224 and 174 km noted previously. The DE3 λ_z is unchanged, and no phase change with height is indicated for DE1. These differences for DE2 and D0 are indicative of the fact that for large $h_{n,s}$ the computation of λ_z is sensitive to the difference between small numbers under the square root sign in Equation 7. Applying the same equation at 112 km with $H = 7.13$ km and $dH/dz = +0.316$, λ_z values of 35, 56, 90, and 55 km are obtained for DE3, DE2, DE1, and D0, respectively (Table 1, column (e)). These represent substantial reductions from the values at 84 km (column (c)), and are in line with the reductions seen in the HME values (compare columns (a) and (d)). It is noted that the absolute LTE values at 112 km are somewhat smaller than the HME values. This is likely due to the λ_z-lengthening influences of dissipation which exist in the HME values but not the LTE values. Since molecular dissipation increases as $\frac{1}{\rho_0}$, at higher altitudes $\lambda_z \rightarrow \infty$, and amplitudes and phases asymptote to constant values in the upper thermosphere.

The above results are robust, not differing substantially when, for example, mean values of H and dH/dz from 65 to 105 km are inserted into Equation 7. Therefore, we are confident in stating that the reductions in λ_z that occur as diurnal tides propagate into the thermosphere are due to the shift in vertical gradient of the background thermal structure from negative to positive at the mesopause. Notably, DE1 is converted from a non-propagating to propagating tide, with enhanced capability to exert vertical coupling within the thermosphere. We now turn to semidiurnal and terdiurnal tides to explore to what degree similar propagation characteristics exist among them.

3.2. Semidiurnal and Terdiurnal HMEs

The work by Forbes et al. (2022) focuses on the htvslat structures of semidiurnal tides determined from ICON/MIGHTI wind measurements between 100 and 280 km, specifically SE2, S0, SW1, SW3, and SW4. SW2 was excluded due to concerns with its extraction form the data owing to aliasing from the zonal mean. Much of that paper was taken up with comparisons between HMEs, the CTMT and the MIGHTI tidal structures, and depictions of legacy HME1-HME4 amp/phzs of these tidal components were in fact provided and in some cases discussed in some depth. One conclusion drawn from these comparisons was that the observed S0, SW1 and SW3 tides above ∼200 km likely contain contributions from in-situ sources, as suggested by the modeling work of Jones et al. (2013). The point was also made that interpretation of semidiurnal tides in terms of HMEs (with the exception of SW4) is more complex than, for example, diurnal tides, due to the fact that generally more than two HMEs are needed to characterize the totality of their htvslat structures. This results from the fact that HME1 → HME4 converges more slowly with respect to reaching the ∼30-km cutoff for significant vertical penetration into the thermosphere than is the case for diurnal tides. In order to avoid redundancy with Forbes et al. (2022), the current presentation and discussion of semidiurnal HMEs focuses on SW2, and aspects of SE2 and SW4 that complement the Forbes et al. (2022) discussions. In fact, results obtained from the following discussion of SW2, SE2, and SW4 HME structures can be extrapolated to all the other semidiurnal tides documented in the Supporting Information S2 based solely on their λ_z; that is, results from SW2(SE2) are broadly representative of those pertaining to SW1, SW3 (S0, SE1, and SE3). This will be understood when it is seen how easily the discussion of semidiurnal and terdiurnal tides follows from that of the diurnal tides.

In the wider context, the relevance of SW2 propagation characteristics to those of the lunar semidiurnal tide (M_2) should be mentioned. Since M_2 and SW2 have identical $s = 2$ zonal wavenumbers and nearly the same periods (12.42 vs. 12.00 hr), their HMs and λ_z from classical theory are nearly the same, and by extension SW2 HMEs represent good approximations to M_2 HMEs and can therefore be useful for lunar tidal studies. The reader is also reminded that SW2 likely possesses a significant component generated in-situ in the thermosphere that increases with solar EUV flux. The same is true for TW3, except that some of the in-situ-generated contribution for TW3 arises from DW1 × SW2 nonlinear interaction involving both the neutral atmosphere and ion drag, both of which also increase with EUV solar flux. To the point, the HMEs revealed here only pertain to those components of SW2 and TW3 that originate from forcing below about 100 km.

The htvslat structures of temperature amp/phzs of the first four HMEs of SW2 and TW3 corresponding to F10.7 = 125 sfu are depicted in Figure 5. The figure is organized in a way such that semidiurnal and terdiurnal amp/phzs for HME1 and HME2 can be compared in the top two rows, and HME3 and HME4 similarly compared in the lower two rows. Table 2 provides various estimates of λ_z for all of the semidiurnal and terdiurnal HMEs documented in this work, in some cases extending out to HME6. Comparing with Table 1 which pertains to diurnal tides, it is immediately evident that the number of HMEs potentially penetrating into the thermosphere (i.e., $\lambda_z \gg 30$ km) for each semidiurnal tidal component is significantly greater than the 1 or 2 HMEs for each diurnal tide.

Given the range of λ_z in Table 2, and the number of latitudinal maxima depicted in Figure 5 (i.e., HME1, HME2, HME3 and HME4 in the sequence of panels (a), (c), (i), and (k) in Figure 5, and implied for higher order HMEs), the htvslat structures of semidiurnal tides in the actual thermosphere are likely to be considerably more complex than those for the diurnal tides, especially below ∼170 km where amplitudes of high-order HMEs tend to be confined. In the vicinity of 200 km and above, the influences of high-order HMEs should generally give way to those of lower-order longer-λ_z HMEs, resulting in less complex latitudinal structures at the higher altitudes. This evolution with height is in fact seen in the semidiurnal tides derived from ICON data and reported by Forbes et al. (2022). Of course, the relative importance of different HME components in observational data also depends on the relative forcing associated with each one.

Comparison of Figure 5 with Figures 2 and 3 reveals that several of the amp/phzs characteristics of diurnal tides noted previously also translate to semidiurnal and terdiurnal tides. Phase structures of SW2 HME1 (panel (b)) and HME1, HME2, HME3 for TW3 (panels (f), (h), and (n)) are very long in the mesosphere, shorten precipitously around 100 km altitude, and then increase with height similar to the thermospheric phase behaviors of DE2, DE1, and D0. λ_z for all of the SW2 and TW3 HMEs depicted in Figure 5 also increase with increasing latitude. It is noteworthy that for each individual HME depicted in Figure 5, that the terdiurnal tides reflect the greatest penetration to higher altitudes, accompanied by significantly larger amplitudes. (Recall that all the tides illustrated in this paper are normalized to a maximum value of 10 K at 98 km.) One factor at play is that the level of dissipation experienced by the tide is inversely proportional to wave period. The shorter-period terdiurnal tide experiences 2/3 the dissipation as a semidiurnal tide with the same λ_z. However, molecular dissipation is proportional to $1/\lambda_z^2$. If one compares the terdiurnal and semidiurnal phase plots for each individual HME in Figure 5,

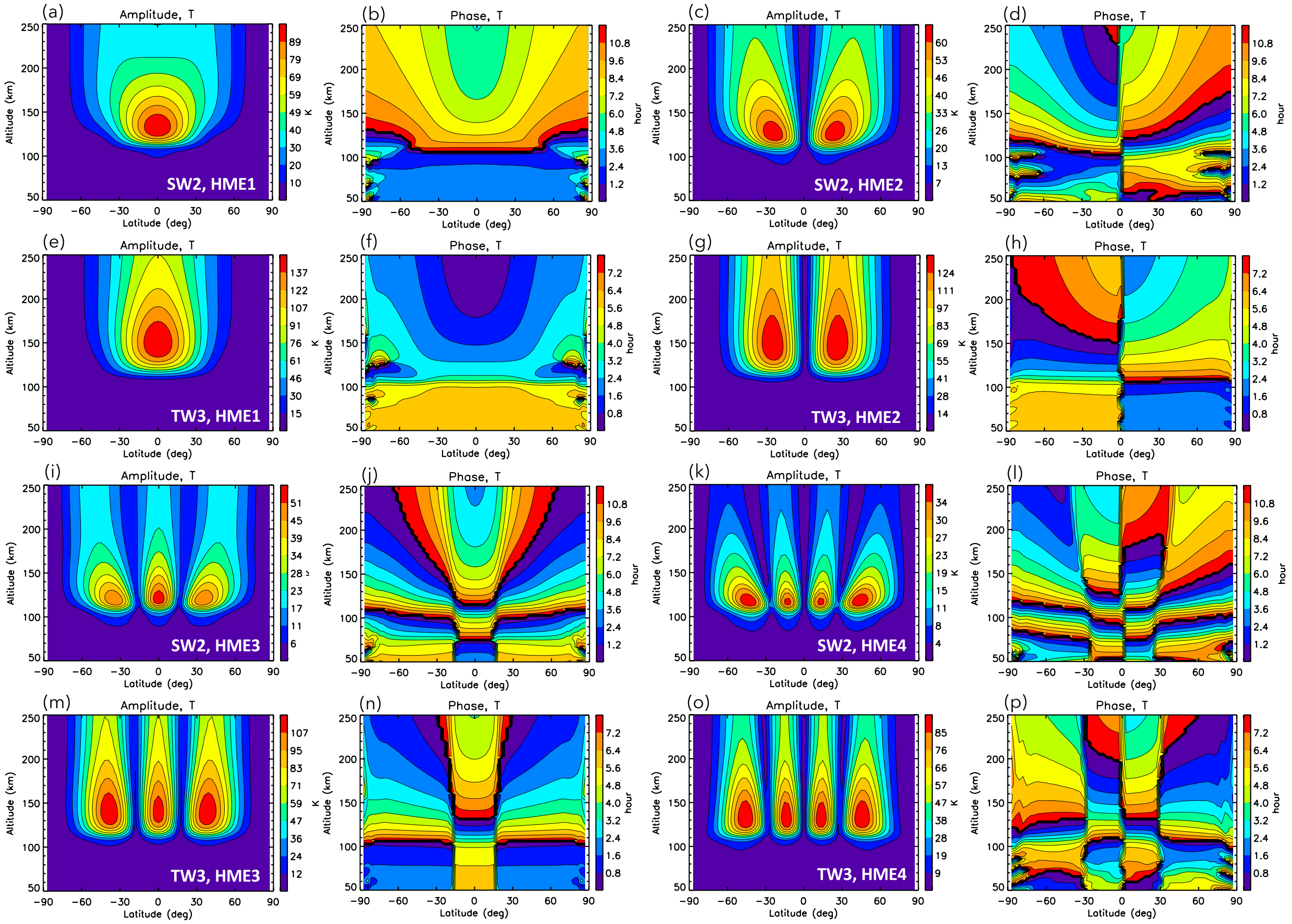

Figure 5. Height versus latitude distributions of the first four temperature Hough Mode Extensions (HMEs) for SW2 and TW3 for F10.7 = 125 sfu. (a–d): HME1 and HME2 for SW2; (e–h) HME1 and HME2 for TW3; (i–l): HME3 and HME4 for SW2; and (m–p): HME3 and HME4 for TW3.

the comparatively longer λ_z seen for the terdiurnal tide is always accompanied by stronger vertical penetration and increased amplitudes than its semidiurnal counterpart. The relative level of dissipation associated with differences in λ_z for a given HME can be ascertained by taking the ratio of λ_z^2 between the semidiurnal and terdiurnal tides based on the values in Table 2. It will be found that the level of dissipation experienced by the longer-λ_z terdiurnal tide is always much smaller than the 2/3's factor ascribable to differences in tidal period.

Table 2
SE2, SW2, SW4, and TW3 λ_z > 30 km Based on Hough Mode Extension (HME) U Phases Over 70–98 km ("84 km") Compared With Those Based on Equation 7 in the Text for a Non-Isothermal Atmosphere, and Those Calculated Based on Equivalent Depths From Laplace's Tidal Equation (LTE) for a T_0 = 256 K Isothermal Background Atmosphere

	SE2			SW2			SW4			TW3		
Tide	HME	LTE 256 K	LTE	HME	LTE 256 K	LTE	HME	LTE 256 K	LTE	HME	LTE 256 K	LTE
HME1	1,867	∞	∞	1,159	316	∞	71	72	81	∞	∞	∞
HME2	781	183	∞	85	82	97	51	50	52	1,244	275	∞
HME3	82	77	88	57	54	57	38	39	40	350	114	190
HME4	55	52	55	40	41	42	31	32	32	75	81	96
HME5	38	40	41	32	34	33				59	64	70
HME6	31	33	33							51	54	57

Note. ∞ implies no phase progression with height.

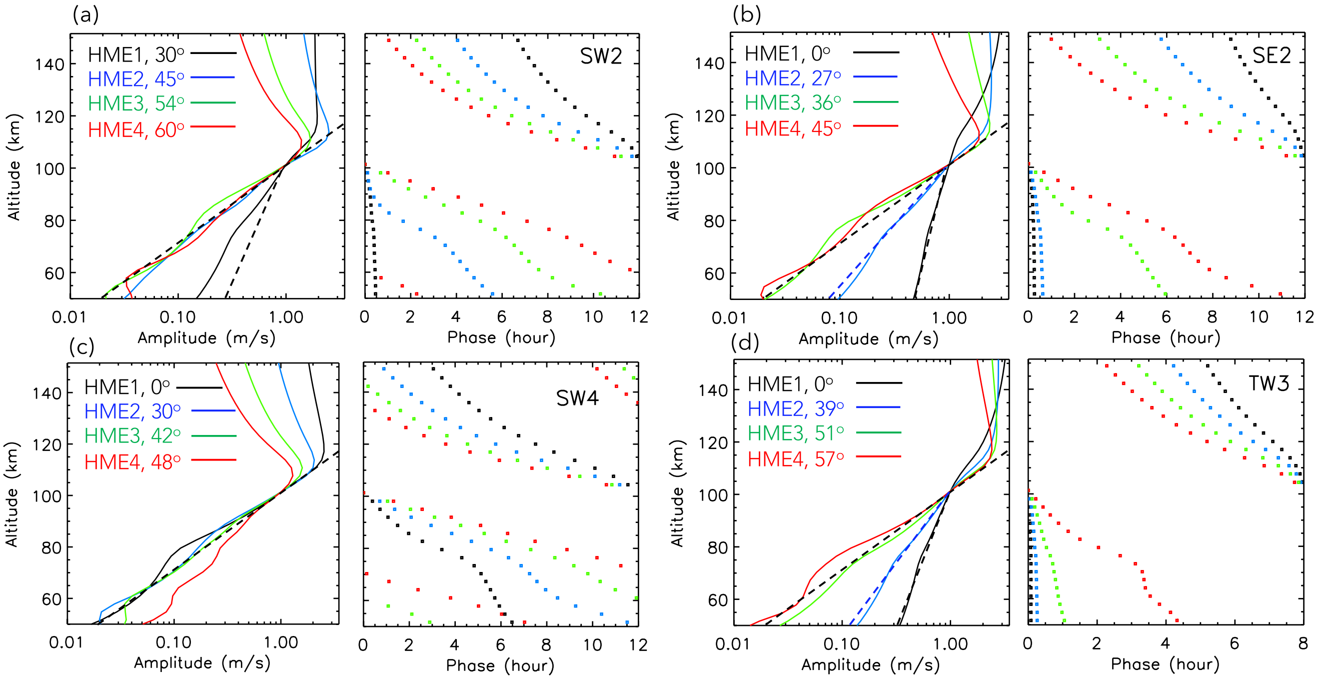

Figure 6. Amplitude and phase vertical profiles of U corresponding to F10.7 = 125 sfu for HME1, HME2, HME3, and HME4 for (a) SW2; (b) SE2; (c) SW4; and (d) TW3. Amplitudes are normalized to unity and phases are normalized to 0000 hr at 102 km, at the latitudes where maximum amplitudes occur, as indicated in each amplitude panel.

Figure 6 is the complement of Figure 4 for the diurnal tides, and provides depictions of U vertical profiles of amp/phz for the first four HMEs of SW2, SE2, SW4, and TW3 corresponding to F10.7 = 125 sfu. The phases illustrated here were used to compute the λ_z at the nominal height of 84 km listed under the heading "HME" in Table 2. Analogous with DE1 in Figure 4, we see that there are occurrences where vertical amplitude structures corresponding to long λ_z are such that vertical growth below 100 km is reduced compared with the $\exp(z/2H)$ growth of shorter-λ_z tidal modes: HME1 for SW2, HME1 and HME2 for SE2 and TW3, and to some degree HME3 for TW3. In each case, the reduced growths follow the dashed lines predicted by classical tidal theory. For each of these tides, their long λ_z shift to much smaller values near 100 km, and HME1 emerges as the largest-amplitude HME at 150 km; this observation comes with the reminder that all HMEs are normalized to unity at 102 km. In Figure 6 HME4 for SW4 also has reduced growth, but in this case reflects the influence of K_{eddy} for this 30 km-λ_z tide, analogous to HME2 for DE3 in Figure 4.

Referring to Table 2, it is seen that for long-λ_z waves (i.e., HME1 and HME2 for SE2; HME1 for SW2; and HME1, HME2 and HME3 for TW3), their λ_z differ considerably between those calculated based on an isothermal T_0 (columns labeled "LTE 256 K"), and those based on a more realistic height-dependent T_0 in the 70–98 km region (columns labeled "LTE"), whereas this is not true for waves with $\lambda_z \lesssim 90$ km. This is related to the sensitivity noted previously regarding the calculation of λ_z for large-$h_{n,s}$, which arises from taking differences between small numbers under the square root sign in Equation 7. It appears that this sensitivity to thermal structure can also be manifested in the actual thermosphere, which impacts the universal application of long-λ_z HMEs based on a single annual-mean thermal structure. For instance, in his study of the M_2 tide, Geller (1970) noted that $\kappa + \frac{dH}{dz}$ varied such that it produced an enhanced "mesospheric barrier" to vertical propagation of the first symmetric mode of M_2 during Northern Hemisphere summer months (N.B., beyond that of the curtailed growth indicated by HME1 for SW2 in Figure 6). This effect can also be seen in the July simulation of the more recent M_2 numerical simulation conducted by Forbes et al. (2013), as compared with, for example, October and January. It implies that the user of HMEs needs to be cognizant of the possibility that low-order long-λ_zHMEs calculated under the simplifying assumption of a background atmosphere single vertical profile may not be universally applicable to all atmospheric realizations.

There is an additional feature of the diurnal and semidiurnal vertical profiles in Figures 4 and 6 that is worthy of comment. That is, the amplitudes reach maximum values at progressively greater altitudes with increasing vertical wavelength. This can be understood by noting that molecular viscosity(thermal conductivity) time scales in the horizontal momentum(thermal energy) equations are of the order of the wave period when

$$\chi = \psi \frac{4\pi^2}{\lambda_z^2} \frac{\mu_0}{\rho_0 n\Omega} \sim 1 \tag{8}$$

where μ_0 is the coefficient of molecular viscosity. The Eucken formula from the kinetic theory of gases relates μ_0 with the coefficient of molecular thermal conductivity, K_0 (Forbes, 1982). Correspondingly, Equation 8 applies with $\psi = 1.0$ for the momentum equations, and $\psi = 1.9$ in the thermal energy equation, where it is assumed that N_2 is the major constituent. (Depending on season and level of solar activity, N_2 is the major constituent between ∼160 and 220 km altitude (Yu et al., 2020). For O, $\psi = 1.5$). According to Equation 8, a wave with a longer λ_z must propagate to a higher altitude to experience the same level of dissipation as a shorter-λ_z wave, all other things being equal. Note also that $\chi \sim 1$ occurs at a somewhat higher altitude in the thermal energy equation, which seems to account for the fact that HME temperatures generally peak at a higher altitudes than HME eastward winds. For example, this height difference is 6 km for HME1 of DE3 and 12 km for HME2 of SW2, independent of F10.7.

Further insight can be gained through reference to the early analytic work by Lindzen (1968), wherein he investigated the vertical propagation of gravity-wave analogs to tides in an isothermal atmosphere whose dissipative time scale increases as $1/\rho_0$. He showed that the shape of the profile above the peak is determined by the quantity $\beta = 2\pi H_D/\lambda_z$, where H_D is the scale height for increase in dissipation. Specifically, for very small $\beta(\lesssim 2)$, wave amplitudes increase roughly as $\exp(z/2H)$ to the level where $\chi \sim 1$, asymptotically approaching a constant above this level with little or no decrease in amplitude. For $\beta \gtrsim 2$, waves reach a peak near the $\chi \sim 1$ level, but then decrease considerably before asymptoting to a constant. Lindzen (1970) soon after noted the complications that come with a non-isothermal thermosphere. Moreover, he did not consider the deviations from $\exp(z/2H)$ exponential growth from long-λ_z waves that occur below 100 km, nor the change in λ_z with height above the mesopause noted previously. Nevertheless, one can see the salient features of Lindzen's predictions in the amplitude profiles of Figures 4 and 6. For instance, HME1 for SW2, HME2 for SE2 and TW3, and HME3 for TW3 conform to the "very small" β behavior for long-λ_z waves. For somewhat smaller λ_z (HME1 for DE2, HME2 for SE2, HME3 for SE2, HME1 for SW4, and HME4 for TW3) there is a slight turning toward smaller amplitudes above the peak. And, for progressively smaller λ_z, the decrease in amplitude above the peak becomes progressively greater; a nice example is the HME1 → HME4 sequence for SW4.

It is important to note that except for the very longest-λ_z tides discussed in connection with Figures 4 and 6, that the ion drag coefficient $\epsilon_0 \sim \Omega$ between 145 and 160 km, and that $\epsilon_0 \sim 2\Omega$ at altitudes at $\gtrsim$170 km (refer to Figure 1). Therefore, ion drag does not appear to be violating the assumption of exponentially increasing dissipation with height that underlies the predictions made in the previous paragraph with respect to tidal behavior below 150 km. However, from Figure 1 it is seen that above these altitudes (and including a region below 250 km), that ion drag terms in the momentum equation can be of the same order as the $\partial/\partial t$ terms, and can therefore play a role in determining tidal behavior. The role of ion drag is explored in the next subsection.

3.3. Dependence on Solar Flux and the Role of Ion Drag

In this subsection, the influences of ion drag and variable solar flux conditions on the behaviors of HMEs are briefly explored. By extension, new insights into tidal propagation in the real atmosphere and the underlying driving factors ought to emerge. However, it is important not to overestimate the capabilities of HMEs, with expectations that some level of *detail* regarding the behavior of tides in the thermosphere can be emulated. The purpose here is to reveal the broad characteristics that are imposed by the background propagation environment (i.e., mean temperature and density, molecular dissipation, ion drag), at the same time realizing that we have much more confidence in specifying the propagation environment than our current knowledge of tidal behavior in the thermosphere. For example, we know how H and ρ_0 both increase with increasing solar flux; so what are the resulting impacts on solar tides that are directly attributable? And, how do HMEs change if ion drag is omitted in their calculation (i.e., $\epsilon_0 = 0$)? We furthermore note from Figure 1 that both the amplitude and altitude of

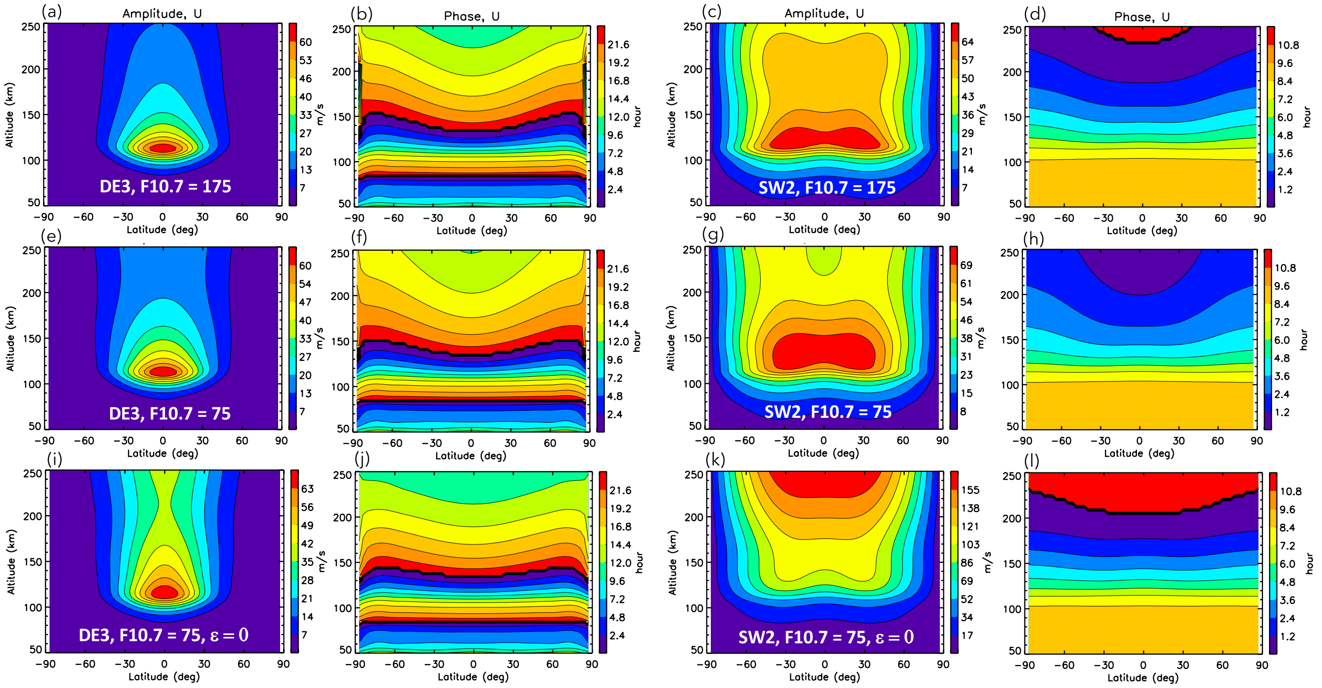

Figure 7. Height versus latitude depictions of amplitude and phase of U for HME1 of DE3 (left two columns) and SW2 (right two columns). Top row: F10.7 = 175 sfu. Middle row: F10.7 = 75 sfu. Bottom row: F10.7 = 75 sfu with $\epsilon_0 = 0$ (i.e., zero ion drag).

maximum ϵ_0 increase with increasing solar flux. So, what do these features of the ionosphere imply with respect to tidal propagation and solar flux variability?

In the following, the specific examples of DE3 and SW2 are examined. DE3 HME1, with λ_z ~60 km is typical of tides in the λ_z range of 50–80 km that propagate non-negligibly to high levels of the thermosphere, and thus intuitively are affected to some degree by ion drag. Tides with λ_z significantly less than 50 km are more or less confined to the lower thermosphere, and the effects of ion drag are inconsequential to their basic existence and impacts. SW2 HME1 can be considered typical of those tides with lower-thermosphere λ_z significantly in excess of 100 km that penetrate effectively to the highest levels of the thermosphere, and are likely to be more profoundly affected by ion drag.

We begin with Figures 7a–7h, wherein U amp/phzs for DE3 ((a) and (b)) and SW2 ((c) and (d)) for F10.7 = 175 sfu (SSMAX) are compared with their F10.7 = 75 sfu (SSMIN) counterparts in panels (e and f) and (g and h), respectively. The SW2 equatorial peak amplitudes for F10.7 = 75(175) sfu are 74(66) ms^{-1} at 136(123) km, while the equatorial amplitudes at 250 km are ≈ 44 ms^{-1} at both SSMIN and SSMAX. The greater peak amplitude is consistent with the higher peak altitude and exponential growth, and the lower peak altitude at SSMAX is consistent with the fact that $\chi = 1$ for molecular dissipation occurs at a lower altitude at SSMAX than SSMIN. Since SW2 has nearly the same λ_z near the amplitude peak for both SSMIN and SSMAX (see contour spacings in panels (d) and (h)), then β is higher at SSMAX than SSMIN due to its dependence on H. Based on the β-associated behaviors discussed at the end of Section 3.2, the expectation is that the rate of decrease of U with height above the peak would be greater at SSMAX (i.e., larger β). However, this is not the case. The rate of decrease of equatorial U amplitude with height above the peak is 18(26) ms^{-1} per 100 km for SSMAX(SSMIN). The disparity appears to be the result of the large influence of ion drag on these calculations, which is demonstrated in Figure 7k. Figure 7k shows the result of the same calculations as in Figure 7g, except that ϵ_0 is set equal to zero. Here the SW2 amplitude reaches 172 ms^{-1} at 250 km and slowly asymptotes to 195 ms^{-1} at 400 km, and exhibits a shorter λ_z (panel (l)) than with ion drag acting (panel (h)). The effect of ion drag on SW2 at these heights is pronounced since at SSMIN ϵ_0 maximizes near 250 km, and in fact exceeds SSMAX values (which maximize near 400 km; see Figure 1) below 270 km.

Table 3

Equatorial Amplitudes of HME1 U and $\Delta\rho/\rho_0$ at 400 km Altitude for DE3 and SW2 for Values of 10.7-cm Solar Flux (F10.7) of 75–200 sfu in Increments of 25 sfu in Rows (a)–(f)

		DE3						SW2					
		(i)	(ii)	(iii)	(iv)	(v)	(vi)	(vii)	(viii)	(ix)	(x)	(xi)	(xii)
F10.7		U	U	$\frac{(ii)}{(i)}$	$\frac{\Delta\rho}{\rho_0}$	$\frac{\Delta\rho}{\rho_0}$	$\frac{(v)}{(iv)}$	U	U	$\frac{(viii)}{(vii)}$	$\frac{\Delta\rho}{\rho_0}$	$\frac{\Delta\rho}{\rho_0}$	$\frac{(xi)}{(x)}$
(sfu)			$\epsilon_0 = 0$			$\epsilon_0 = 0$			$\epsilon_0 = 0$			$\epsilon_0 = 0$	
75	(a)	10.0	21.0	2.1	0.039	0.069	1.8	10.0	43.0	4.3	0.046	0.170	3.7
100	(b)	7.50	17.4	2.3	0.028	0.046	1.6	8.03	39.0	4.9	0.038	0.127	3.3
125	(c)	5.53	14.8	2.7	0.022	0.032	1.5	6.36	35.0	5.5	0.033	0.096	2.9
150	(d)	4.60	12.8	2.8	0.018	0.023	1.3	5.59	29.0	5.4	0.029	0.059	2.0
175	(e)	3.88	11.2	2.9	0.014	0.017	1.2	5.37	29.0	5.4	0.026	0.059	2.3
200	(f)	3.59	9.94	2.8	0.011	0.014	1.3	5.10	28.0	5.5	0.022	0.048	2.2
	$\frac{(a)}{(f)}$	2.8	2.1		3.5	4.9		2.0	1.5		2.1	2.6	

Note. $\epsilon_0 = 0$ means that ion drag was omitted in the Hough Mode Extension (HME) calculations. All results shown are normalized to be internally self-consistent with a U amplitude of 10 m/s at F10.7 = 75 sfu, equivalent to a re-normalization of the HMEs to equatorial temperature amplitudes at 98 km of 4.85 K for DE3 and 2.22 K for SW2.

Our interpretation of the SW2 results in Figure 7 is summarized as follows. Comparing panel (g) (F10.7 = 75 sfu) with panel (k) (F10.7 = 75 sfu; $\epsilon_0 = 0$), the addition of ion drag between 150 and 250 km significantly reduces amplitudes in this region as compared with <150 km, moving maximum amplitudes from $\gtrsim$250 to 136 km (compare (g) to (k)). At the same time, ion drag lengthens λ_z between 150 and 250 km (compare (h) to (l)). Similarly, the enhancement of ion drag experienced within 160–260 km at SSMIN relative to SSMAX (Figure 1) also lengthens λ_z (compare (h) to (d)) and reduces amplitudes (compare (g) to (c)), but not profoundly so. The difference from the $\epsilon_0 =$ situation stems from the fact that it is only the excess in ion drag from the $\epsilon_0 \gtrsim \Omega$ background level of ion drag between 160 and 260 km at SSMAX relative to SSMIN (Figure 1) that produces the differences between those illustrated in panels (g and h) versus those in panels (c and d).

A similar series of results for DE3 U is contained in the left two columns of Figure 7. Comparing panels (e and f) with panels (i and j), we see that the addition of ion drag lengthens λ_z and reduces equatorial amplitudes above the peak, from 37.5 to 17.8 ms^{-1} at 250 km. Ion drag thus has the effect of reducing DE3 equatorial amplitudes at 250 km by a factor of 2 (compared with the absence of ion drag), whereas the reduction is nearly a factor of 4 for SW2. The removal of some ion drag between 150 and 250 km (comparing panels (a and b) with panels (e and f), remembering that ion drag is less for SSMAX than SSMIN in this region; cf., Figure 1) has the effect of decreasing λ_z and reducing amplitudes at 250 km from 17.8 to 12.7 ms^{-1} at 250 km, whereas little change at 250 km occurred for SW2.

These results point to two conclusions. First, ion drag has a significant damping effect on the overall amplitudes of solar tides, and has the effect of lengthening vertical wavelengths. Ion drag also introduces significant variability with respect to solar cycle. However, as indicated in Figure 1, the solar cycle influence of ion drag varies with height, due to the fact that ion drag maximizes around 250 km at F10.7 = 75 sfu, around 320 km at F10.7 = 125 sfu, and ≥400 km for F10.7 ≥175 sfu. Indeed, between 160 and 260 km, ion drag at SSMIN (i.e., F10.7 = 75 sfu) exceeds that for nominal SSMAX conditions (i.e., F10.7 = 175 sfu). Second, embedded in these results is a complex interplay between the influences of molecular dissipation and ion drag with respect to solar cycle, which makes it difficult to make any more than very general statements that are broadly applicable across the spectrum of diurnal, semidiurnal, and terdiurnal tides of varying wavelengths.

A complementary perspective can be gained by examining results at 400 km for DE3 and SW2, which are summarized in Table 3. The tabulations include HME1 equatorial values for U and $\Delta\rho/\rho_0$ with ($\epsilon_0 \neq 0$) and without ($\epsilon_0 \neq 0$) ion drag included in the calculations, for values of 10.7-cm solar flux (F10.7) of 75–200 sfu in increments of 25 sfu in rows (a–f). DE3 U values are tabulated in column (i), normalized to 10 ms^{-1} at F10.7 = 75 sfu for the present discussion. The value of 10 ms^{-1} is close to the ≈10 to 12 ms^{-1} equatorial (5°S–5°N) value derived from

CHAMP observations at 390 km during SSMIN (F10.7 ≈ 65–75 sfu, August 2006–2008) by Häusler et al. (2012). They show DE3 U to decrease with increasing solar activity, achieving a value of ≈4.5 ms^{-1} in September 2002 (F10.7 ≈ 175 sfu), consistent with the trend and values in column (i) of Table 3. Column (iv) of Table 3 shows the $\Delta\rho/\rho_0$ values that are internally consistent with HME1 of DE3. The values of 0.039 and 0.014 are similar in magnitude with Häusler et al.'s (2012) DE3 observations of ≈ 0.025-0.035 at SSMIN and 0.01 at SSMAX. So, at least in this case, the HME captures the self-consistency between U and $\Delta\rho/\rho_0$ and the solar cycle variability of these parameters in line with actual observations, provided that a proper reference point (i.e., calibration factor) can be applied that is also observation-based. Note that the above normalization to 10 ms^{-1} at F10.7 = 75 sfu is equivalent to a re-normalization of DE3 HME1 to an equatorial temperature amplitude of 4.85 K at 98 km, implying that this might have been a more realistic choice than the arbitrary normalization of 10 K at 98 km.

A similar set of data is provided in columns (vii)–(xii) for HME1 of SW2. Our normalization of SW2 to $U = 10\ \mathrm{ms}^{-1}$ is arbitrary in the sense that we do not know the amplitudes of SW2 arising separately from in-situ excitation versus that propagating from below, but it does allow for a cogent comparison with DE3 results. Some differences compared to DE3 are immediately noticeable. First, referring to columns (ix) for SW2 and (iii) for DE3, the ratio $U(\epsilon_0 = 0)/U$ ranges between 2.1–2.9 for DE3 and 4.3–4.5 for SW2, and increases only slightly from F10.7 = 75 to 125 sfu before plateauing to a near constant value for F10.7 values $\gtrsim$125 sfu for both DE3 and SW2. These differences and similarities are consistent with the fact that molecular dissipation alone ($\epsilon_0 = 0$) does not contribute nearly as much to solar cycle variability of DE3 and SW2 U as ion drag, and that solar cycle variability due to ion drag is complicated by the fact that the amplitude and peak height of ϵ_0 change with solar cycle.

In contrast to U, the density responses of DE3 (columns (iv) and (v)) and SW2 (columns (x) and (xi)) at 400 km decrease monotonically from SSMIN to SSMAX, and are reduced by a smaller factor when ϵ_0 is set equal to zero in the HME calculations (i.e., 1.3–1.8 for DE3 and (column (vi) in Table 3) and 2.2–3.7 for SW2 (column (xii) in Table 3)). Our interpretation is that this is due to the fact that ion drag affects U ad V directly and $\Delta\rho_0/\rho_0$ indirectly. As noted previously, ion drag directly affects U in the eastward momentum equation, less so for V in the southward momentum equation due to the influence of the magnetic dip angle. A related secondary effect of ion drag is to suppress the vertical velocity and the velocity divergence, which leads to suppression of $\Delta\rho_0/\rho_0$ through Equation 5. Note that the coefficient of $\hat{w}$ in Equation 5 reduces to $1/H$ for an isothermal upper thermosphere. Since H increases with solar activity, this factor compounds the suppression of $\Delta\rho_0/\rho_0$ at higher levels of solar activity in the presence of ion drag, and may be a major factor in the absence of ion drag. For example, this may account for the more precipitous declines in the density response with increasing solar activity as compared with U; compare (a)/(f) = 4.9 versus 2.1 (bottom of columns (v) and (ii) for DE3, and 2.6 versus 1.5 (bottom of columns (xi) and (viii)) for SW2 in Table 3.

4. Conclusions

This paper quantifies and interprets how thermosphere dissipation in the form of molecular viscosity, molecular thermal conductivity and collisions with ions ("ion drag") determines the height versus latitude structures of a variety of migrating and non-migrating solar thermal tides, pole-to-pole up to 400 km altitude. This is accomplished through computation of thermosphere HMEs; that is, solutions to the linearized momentum, thermal energy, continuity, state and hydrostatic balance equations wherein the horizontal structure of troposphere forcing for each HME corresponds to the eigenfunction (Hough function) of Laplace's tidal equation for a particular tidal mode, and the background state and thermosphere dissipation are specified for nominal solar minimum (SSMIN), average (SSAVG), and maximum (SSMAX) activity conditions. The broad features revealed, different for each HME, include changes in vertical(horizontal) structure with latitude(height), degree of vertical penetration to the middle and upper thermosphere, changes in vertical wavelength with height due to the transition in background thermal gradient around the mesopause, and the role of ion drag in determining tidal amplitudes and their solar cycle variability. The HMEs are particularly useful for fitting measurements of tides, and for estimating tidal fields beyond those dependent variables actually fit and including those outside the fitting domain. These HMEs were created as part of the ICON mission to serve as observation-based lower boundary conditions for TIEGCM-ICON. The full set of 67 HMEs in tabular and graphical form, each one for solar flux levels of F10.7 = 75, 125, and 175 sfu, are publicly available as part of Supporting Information S2 to this paper. The specific scientific conclusions to emerge from the present work are summarized below.

1. Interaction of a tide with the dissipative thermosphere is primarily determined by its λ_z and secondarily by its wave period; longer(shorter)-λ_z and shorter(longer)-period tides are less(more) susceptible to dissipation and penetrate more(less) effectively to higher levels. This implies that the results discussed in the present paper specifically for DE3, DE2, DE1, D0, SE2, S0, SW2, and TW3, are broadly applicable to similar-wavelength HMEs for SE3, SE1, S0, SW1, and SW3.
2. Variable among the HMEs depending on λ_z, temperatures peak at a somewhat higher altitude than eastward winds. This is apparently due to differences between the time constants for molecular viscosity and thermal conductivity in the momentum and thermal energy equations, respectively.
3. HME southward wind amplitudes tend to peak at a higher altitude than eastward winds, and penetrate more readily to higher altitudes above the peak. This is attributable to the influence of ion drag, which arises through the term $\epsilon_0 U$ in the eastward momentum equation, but is of diminished importance to V in the southward momentum equation (especially at low to middle latitudes) where the magnetic dip angle (I) enters through the term $\epsilon_0 V \sin^2 I$.
4. HMEs with 30 km $\lesssim \lambda_z \lesssim$ 100 km peak in the vicinity of ~130 km, slightly higher(lower) for longer(shorter) λ_z or shorter(longer) periods, and tend to fall off less(more) rapidly above the peak for longer(shorter) λ_z. Waves in this λ_z range grow exponentially with height below the peak at the same $\exp(z/2H)$ rate where z is altitude and H is a mean scale height. HMEs with λ_z ~30 km grow more slowly with height below the peak due to the assumed level of eddy diffusivity, which is not known with specificity. Therefore, there is some uncertainty in the vertical growth of HMEs with λ_z ~30 km below the peak.
5. HMEs with $\lambda_z \gtrsim$100 km grow exponentially with height more slowly than $\exp(z/2H)$, at rates approximately predictable by classical tidal theory. Once exponential growth ceases, such tides tend to approach a constant value with height.
6. The reduced growth with height noted above was alluded to in the context of the first symmetric mode of the lunar semidiurnal tide (M_2) by Geller (1970). M_2 has a period, equivalent depth, HM structure and vertical wavelength close to that of the first symmetric mode or HME1 of SW2. He used the term "mesospheric barrier" to describe the effects of enhanced summertime negative mesospheric lapse rates that lead to pronounced quasi-evanescent behavior and reduced accessibility to the thermosphere. However, the reduced growth rates noted above can occur even for an isothermal atmosphere and sufficiently large equivalent depth. In fact, it is shown here that several low-order HMEs of non-migrating tides prominently observed in the atmosphere possess this reduced-growth characteristic, including HME1 for DE1, SE2, SW2, and TW3, HME2 for SE2 and TW3, HME3 for TW3; and by extension based on their large λ_z, HME1 for SE3, SE1, S0, SW1, SW3, and HME2 for SE1, S0, SW1.
7. For tides that propagate effectively to ~250 km, which includes tides with $\lambda_z \gtrsim$ 50 km based on the results shown here for DE3, broadening of horizontal structures and λ_z lengthening with increasing latitude occurs, consistent with the htvslat inseparability imposed on the tidal equations by the presence of dissipation.
8. It is a common feature of the tides addressed in this paper to undergo a λ_z shortening as they propagate from below the mesopause to ~120 km altitude. It is shown here that this characteristic is tied to the change in the sign of the background temperature lapse rate from negative to positive around the mesopause.
9. The effects of ion drag on solar tidal amplitudes in the thermosphere are large, and are consequential for those tides with $\lambda_z \gtrsim$50 km that propagate non-negligibly to ~250 km and beyond. In numerical experiments with HME1 of DE3 (λ_z ~60 km) and HME1 of SW2 ($\lambda_z \gg$ 100 km), U amplitudes at 400 km increased by factors of ~2 to 3 and ~4 to 6, respectively, when ion drag was set to zero in the HME calculations.
10. The influences of ion drag on the density responses of solar tides are somewhat less than on U. While their SSMIN/SSMAX ratios are larger, increases in their amplitudes when ion drag is omitted in the HME calculations are less; the factors are ~1 to 2 and ~2 to 4 as compared with the values quoted above for DE3 and SW2, respectively. These differences are due in part to the fact the ion drag directly affects U in the eastward momentum equation, whereas the effect on $\Delta\rho_0/\rho_0$ enters indirectly through the continuity equation, and a factor $1/H$ (which decreases from SSMIN to SSMAX) times the vertical velocity that also appears in the expression for $\Delta\rho/\rho_0$.
11. There is a complicating factor in diagnosing ion drag influences on solar tides and making any more than salient statements concerning their solar cycle variability. That is, both the amplitude and altitude of maximum ion drag coefficient (ϵ_0) increase with increasing solar flux. Indeed, within the 150–270 km height region, ϵ_0 is larger at F10.7 = 75 sfu than at F10.7 = 175 sfu due to the differences in the F-layer peak heights at these two levels of solar activity. On the other hand, above about 350 km, ϵ_0 increases monotonically from

F10.7 = 75 to 175 sfu. This means that, depending on its λ_z and latitudinal extent, the solar cycle variability of a HME (or a tide in the real atmosphere) can vary with height or latitude.

In many respects, the current work represents the thermosphere extension of the classical solar tidal results in Chapman and Lindzen (1970). Two-dimensional HMEs replace HMs and velocity expansion functions, and height-dependent λ_z replace single values. As in classical tidal theory, in order to have a universal set of basis functions, the specifications of the background atmosphere and dissipation in the computation of HMEs are latitude-independent. Therefore, the potential influences of zonal-mean eastward winds and latitudinally varying ion drag are omitted. Indeed, little is known about the diurnal-mean wind field between 100 and 250 km, since day and night measurements do not exist over most of this height regime. However, it is known that in the actual atmosphere, Doppler shift effects (e.g., Gasperini et al., 2017) and the meridional gradients of mean winds (e.g., McLandress, 2002) can potentially influence the latitudinal and vertical structures of tides.

Finally, care must be taken in terms of how HMEs are utilized. Given the simplifications underlying their creation, one must be cognizant of their shortcomings and limitations. For example, it is important not to expect that HMEs will emulate any more than the salient behaviors of tides in the thermosphere. Moreover, HME fitting to tidal observations requires adequate constraints to define the presence of any given HME. This means that sufficient coverage in latitude, and possibly the simultaneous fitting to multiple tidal fields (i.e., u, v, T) to constrain the fit in the absence of extensive latitude coverage, are generally required. Often, only a few HMEs can be fit simultaneously, and post-facto comparisons between reconstructions based on the fit and the observational data are necessary to confirm the veracity of the final product. Another good practice is to apply HME fitting to proxy data such as a GCM, where the true solution is known, to verify the adequacy of any given set of data constraints (see e.g., Svoboda et al., 2005).

Data Availability Statement

The Hough Mode and Hough Mode Extension data sets pertinent to this paper can be found at https://doi.org/10.5281/zenodo.7150798 (Forbes & Zhang, 2022).

Acknowledgments
This work was funded by the ICON mission, which is supported by the NASA's Explorers Program through contracts NNG12FA45C and NNG12FA42I. The LTE solver used to generate Hough functions and eigenvalues was developed by Scott E. Palo, and shared with us as part of previous collaborations, particularly Truskowski et al. (2014); his contributions to that part of the current work are acknowledged.

References

Chapman, S., & Lindzen, R. S. (1970). *Atmospheric tides*. D. Reidel.

Chiu, Y. T. (1975). An improved Phenomenological model of ionospheric density. *Journal of Atmospheric and Terrestrial Physics*, *37*(12), 1563–1570. https://doi.org/10.1016/0021-9169(75)90035-5

Cullens, C. Y., Immel, T. J., Triplett, C. C., Wu, Y. J., England, S. L., Forbes, J. M., & Liu, G. (2020). Sensitivity study for ICON tidal analysis. *Progress in Earth and Planetary Science*, *7*(1), 18. https://doi.org/10.1186/s40645-020-00330-6

Emmert, J. T., Drob, D. P., Picone, J. M., Siskind, D. E., Jones, M., Jr., Mlynczak, M. G., et al. (2020). NRLMSIS 2.0: A whole atmosphere empirical model of temperature and neutral species densities. *Earth and Space Science*, *7*(3), e2020EA001321. https://doi.org/10.1029/2020EA001321

Flattery, T. W. (1967). *Hough functions* (Technical Report No. 21). Department of Geophysical Sciences, University of Chicago.

Forbes, J. M. (1982). Atmospheric tides. I. Model description and results for the solar diurnal component. *Journal of Geophysical Research*, *87*(A7), 5222–5240. https://doi.org/10.1029/JA087iA07p05222

Forbes, J. M. (2000). Wave coupling between the lower and upper atmosphere: Case study of an ultra-fast Kelvin wave. *Journal of Atmospheric and Solar-Terrestrial Physics*, *62*(17–18), 1603–1621. https://doi.org/10.1016/S1364-6826(00)00115-2

Forbes, J. M. (2021). Atmosphere-ionosphere (A-I) coupling by solar and lunar tides. In W. Wang, Y. Zhang, & L. J. Paxton (Eds.), *Space physics and aeronomy, volume 4, upper atmosphere dynamics and energetics* (Vol. 560). American Geophysical Union.

Forbes, J. M., & Garrett, H. B. (1979). Theoretical studies of atmospheric tides. *Reviews of Geophysics*, *17*(8), 1951–1981. https://doi.org/10.1029/RG017i008p01951

Forbes, J. M., & Hagan, M. E. (1982). Thermospheric extensions of the classical expansion functions for semidiurnal tides. *Journal of Geophysical Research*, *87*(A7), 5253–5259. https://doi.org/10.1029/JA087iA07p05253

Forbes, J. M., He, M., Maute, A., & Zhang, X. (2020). Ultrafast Kelvin wave variations in the surface magnetic field. *Journal of Geophysical Research: Space Physics*, *125*(9), e2020JA028488. https://doi.org/10.1029/2020JA028488

Forbes, J. M., Maute, A., & Zhang, X. (2020). Dynamics and electrodynamics of an ultra-fast Kelvin wave (UFKW) packet in the ionosphere-thermosphere (IT). *Journal of Geophysical Research: Space Physics*, *125*(5), e2020JA027856. https://doi.org/10.1029/2020JA027856

Forbes, J. M., Oberheide, J., Zhang, X., Cullens, C., Englert, C. R., Harding, B. J., et al. (2022). Vertical coupling by solar semidiurnal tides in the thermosphere from ICON/MIGHTI measurements. *Journal of Geophysical Research: Space Physics*, *127*(5), e2022JA030288. https://doi.org/10.1029/2022JA030288

Forbes, J. M., & Vial, F. (1991). Semidiurnal tidal climatology of the E region. *Journal of Geophysical Research*, *96*(A2), 1147–1157. https://doi.org/10.1029/90JA02187

Forbes, J. M., & Zhang, X. (2022). Thermosphere Hough mode extensions (HMEs) for solar tides in Earth's atmosphere [Dataset]. https://doi.org/10.5281/zenodo.7150798

Forbes, J. M., Zhang, X., Bruinsma, S., & Oberheide, J. (2013). Lunar semidiurnal tide in the thermosphere under solar minimum conditions. *Journal of Geophysical Research: Space Physics*, *118*(4), 1–14. https://doi.org/10.1029/2012JA017962

Forbes, J. M., Zhang, X., Hagan, M. E., England, S. L., Liu, G., & Gasperini, F. (2017). On the specification of upward-propagating tides for ICON science Investigations. *Space Science Reviews*, *212*(1–2), 697–713. https://doi.org/10.1007/s11214-017-0401-5

Forbes, J. M., Zhang, X., Heelis, R., Stoneback, R., Englert, C. R., Harlander, J. M., et al. (2021). Atmosphere-ionosphere (A-I) coupling as viewed by ICON: Day-to-day variability due to planetary wave (PW)-tide interactions. *Journal of Geophysical Research: Space Physics*, *126*(6), e2020JA028927. https://doi.org/10.1029/2020JA028927

Gasperini, F., Forbes, J. M., & Hagan, M. E. (2017). Wave coupling from the lower to the middle thermosphere: Effects of mean winds and dissipation. *Journal of Geophysical Research: Space Physics*, *122*(7), 7781–7797. https://doi.org/10.1002/2017JA024317

Geller, M. A. (1970). An investigation of the lunar semidiurnal tide in the atmosphere. *Journal of the Atmospheric Sciences*, *27*(2), 202–218. https://doi.org/10.1175/1520-0469(1970)027<0202:AIOTLS>2.0.CO;2

Gu, S.-Y., Dou, X., Lei, J., Li, T., Luan, L., Wan, W., & Russell, J. M., III (2014). Ionospheric response to the ultrafast Kelvin wave in the MLT region. *Journal of Geophysical Research: Space Physics*, *119*(2), 1369–1380. https://doi.org/10.1002/2013JA019086

Häusler, K., Oberheide, J., Lühr, H., & Koppmann, R. (2012). The geospace response to nonmigrating tides. In F.-J. Lübken (Ed.), *Climate and weather of the Sun-Earth System (CAWSES): Highlights from a priority Program* (pp. 481–506). Springer Atmospheric Sciences. https://doi.org/10.1007/978-94-007-4348-9

Hernandez, G., Fraser, G. J., & Smith, R. W. (1993). Mesospheric 12-hour oscillations near South Pole, Antarctica. *Geophysical Research Letters*, *20*(17), 1787–1790. https://doi.org/10.1029/93GL01983

Hernandez, G., Smith, R. W., Fraser, G. J., & Jones, W. L. (1992). Large-scale waves in the upper mesosphere at Antarctic high latitudes. *Geophysical Research Letters*, *19*(13), 1347–1350. https://doi.org/10.1029/92GL01281

Jones, M., Jr., Forbes, J. M., Hagan, M. E., & Maute, A. (2013). Non-migrating tides in the ionosphere-thermosphere: In situ versus tropospheric sources. *Journal of Geophysical Research: Space Physics*, *118*(5), 2438–2451. https://doi.org/10.1002/jgra.50257

Lindzen, R. S. (1968). Vertically propagating waves in an atmosphere with Newtonian cooling inversely proportional to density. *Canadian Journal of Physics*, *46*(16), 1835–1840. https://doi.org/10.1139/p68-520

Lindzen, R. S. (1970). Internal gravity waves in atmospheres with realistic dissipation and temperature, part I. Mathematical development and propagation of waves into the thermosphere. *Geophysical Fluid Dynamics*, *1*(3–4), 303–355. https://doi.org/10.1080/03091927009365777

Lindzen, R. S., & Forbes, J. M. (1983). Turbulence originating from convectively stable internal waves. *Journal of Geophysical Research*, *88*(C11), 6549–6553. https://doi.org/10.1029/JC088iC11p06549

Lindzen, R. S., Hong, S. S., & Forbes, J. M. (1977). *Semidiurnal Hough mode extensions in the thermosphere and their application* (Memorandum Report 3442). Naval Research Laboratory.

Liu, G., England, S. L., Immel, T. J., Frey, H. U., Mannucci, A. J., & Mitchell, N. J. (2015). A comprehensive survey of atmospheric quasi 3 day planetary-scale waves and their impacts on the day-to-day variations of the equatorial ionosphere. *Journal of Geophysical Research: Space Physics*, *120*(4), 2979–2992. https://doi.org/10.1002/2014JA020805

Longuet-Higgins, M. S. (1968). The eigenfunctions of Laplace's tidal equations over a sphere. *Philosophical Transactions of the Royal Society of London – Series A: Mathematical and Physical Sciences*, *262*(1132), 511–607. https://doi.org/10.1098/rsta.1968.0003

Maute, A. (2017). Thermosphere-ionosphere-electrodynamics general circulation model for the ionospheric connection explorer: TIEGCM-ICON. *Space Science Reviews*, *212*(1–2), 523–551. https://doi.org/10.1007/s11214-017-0330-3

McLandress, C. (2002). The seasonal variation of the propagating diurnal tide in the mesosphere and lower thermosphere: Part II. The role of tidal heating and zonal mean winds. *Journal of the Atmospheric Sciences*, *59*(5), 907–922. https://doi.org/10.1175/1520-0469(2002)059<0907:TSVOTP>2.0.CO;2

Oberheide, J., Forbes, J. M., Häusler, K., Wu, Q., & Bruinsma, S. L. (2009). Tropospheric tides from 80 to 400 km: Propagation, interannual variability, and solar cycle effects. *Journal of Geophysical Research*, *114*(D1), D00I05. https://doi.org/10.1029/2009JD012388

Oberheide, J., Forbes, J. M., Zhang, X., & Bruinsma, S. L. (2011). Climatology of upward propagating diurnal and semidiurnal tides in the thermosphere. *Journal of Geophysical Research*, *116*(A11), A11306. https://doi.org/10.1029/2011JA016784

Pancheva, D., Mukhtarov, P., Siskind, D. E., & Smith, A. K. (2016). Global distribution and variability of quasi 2-day waves based on the NOGAPS-ALPHA reanalysis model. *Journal of Geophysical Research: Space Physics*, *121*(11), 11422–11449. https://doi.org/10.1002/2016JA023381

Rishbeth, H., & Garriott, O. K. (1969). *Introduction to ionospheric physics* (pp iii–vii and 1–331). Academic Press.

Salby, M. L., Hartmann, D. L., Bailey, P. L., & Gille, J. C. (1984). Evidence for equatorial Kelvin modes in nimbus-7 LIMS. *Journal of the Atmospheric Sciences*, *41*(2), 220–235. https://doi.org/10.1175/1520-0469(1984)041<0220:EFEKMI>2.0.CO;2

Svoboda, A. A., Forbes, J. M., & Miyahara, S. (2005). A space-based climatology of diurnal MLT tidal winds, temperatures and densities from UARS wind measurements. *Journal of Atmospheric and Solar-Terrestrial Physics*, *67*(16), 1533–1543. https://doi.org/10.1016/j.jastp.2005.08.018

Truskowski, A. O., Forbes, J. M., Zhang, X., & Palo, S. E. (2014). New perspectives on thermosphere tides – 1. Lower thermosphere spectra and seasonal-latitudinal structures. *Earth Planets and Space*, *66*, 136. https://doi.org/10.1186/s40623-014-0136-4

Vlasov, M. N., & Kelley, M. C. (2015). Eddy diffusion coefficients and their upper limits based on application of the similarity theory. *Annales Geophysicae*, *33*(7), 857–864. https://doi.org/10.5194/angeo-33-857-2015

Yu, T., Ren, Z., Yu, Y., Yue, X., Zhou, X., & Wan, W. (2020). Comparison of reference heights of O/N_2 and $\Sigma O/N_2$ based on GUVI dayside limb measurement. *Space Weather*, *18*(1), e2019SW002391. https://doi.org/10.1029/2019SW002391